

# Recent advances in ternary two dimensional materials: synthesis, properties and applications

Lina Wang<sup>a,b</sup>, Peng Hu<sup>c\*</sup>, Yi Long<sup>c</sup>, Zheng Liu<sup>c,d\*</sup> and Xuexia He<sup>a,b\*</sup>

Two-dimensional (2D) materials have gained significant attention owing to their unique physical and chemical properties, which arise mainly from their high surface-bulk ratios and topological effects. Since the discovery of graphene in 2004, the family of 2D materials has expanded rapidly. Thus far, several single-element 2D materials (graphene, phosphorene, etc.) have been reported; the majority contain two (MoS<sub>2</sub>, WSe<sub>2</sub>, etc.) or more elements (Mo<sub>2</sub>CT<sub>x</sub>, CrPS<sub>4</sub>, Bi<sub>2</sub>Sr<sub>2</sub>CaCu<sub>2</sub>O<sub>x</sub>, etc.). Of these, three-element 2D materials, also called ternary 2D materials, represent a rather attractive direction of recent years. Typical ternary 2D materials include metal phosphorous trichalcogenides (MPTs), ternary transition metal chalcogenide (TMDs), transition metal carbides and nitrides (MXene) and 2D ternary oxides. Ternary 2D systems result in multiple degrees of freedom to tailor physical properties via stoichiometric variation. Moreover, they exhibit some properties not characteristic of binary 2D systems, such as band gap tuning. In this paper, we have reviewed the recent progress on various ternary 2D materials on the basis of their classification (MPTs, ternary 2D MXene, ternary TMDs, BCN and other ternary 2D materials.). The synthesis methods, structures, key properties (such as band gap tuning, phase transition and topological phase), and their applications, are summarized. In addition, the strategies to tackle challenges, as well as the outlooks of this field, are presented.

## 1 Introduction

Since the discovery of graphene in 2004,<sup>1</sup> atomically thin two-dimensional (2D) materials have attracted considerable interest owing to their unprecedented physical, chemical and electronic properties.<sup>2</sup> They have shown great potential in various applications in electronic, optoelectronic devices, catalysis, sensors and energy storage devices.<sup>3-11</sup> Prompted by the increasing research on graphene, researchers have started to explore and isolate other layered materials. After decades' of progress, various 2D materials have been reported, including MoS<sub>2</sub>, h-BN, WTe<sub>2</sub>, germanene and black phosphorus.<sup>12-19</sup> Note that the physical, chemical and electronic properties of 2D materials are versatile and material-dependent, making each of them favorable for specific applications.<sup>13, 14, 20</sup> For example, the structure of h-BN is similar to that of graphene. However, unlike graphene, h-BN is an insulator, with a band gap larger than 5 eV. The band gap of single-layered h-BN could be up to 6 eV. Most importantly, h-BN is resistant to chemical attack and harsh conditions such as high temperature.<sup>14, 21, 22</sup> Therefore, the exploration of new 2D materials with interesting novel properties is crucial for building the landscape of the 2D world and thus, leading to fascinating applications.

Currently, research on 2D materials has been almost exclusively focused on single elements, such as graphene and black phosphorus and on binary systems such as MoS<sub>2</sub> and WS<sub>2</sub>. A majority of the 2D materials are binary systems.<sup>14, 15</sup> In addition, efforts have been devoted to the discovery of new 2D materials, to meet the requirements of future electronic and optoelectronic technologies. Therefore, 2D materials with multiple elements, such as Mo<sub>2</sub>CT<sub>x</sub>, CrPS<sub>4</sub> and Bi<sub>2</sub>Sr<sub>2</sub>CaCu<sub>2</sub>O<sub>x</sub>, have also been reported recently.<sup>23, 24</sup> Among these, three-element 2D materials, also called ternary 2D materials, represent a rather attractive research direction. Typical ternary 2D materials include metal phosphorous trichalcogenides (MPT: MnPS<sub>3</sub>, CrPS<sub>4</sub>, FePSe<sub>3</sub>, etc.), ternary transition metal carbides, carbonitrides and nitrides (MXenes: Ta<sub>6</sub>AlC<sub>5</sub> and Ti<sub>7</sub>SnC<sub>6</sub>), and ternary transition metal dichalcogenides (TMDs: Mo<sub>x</sub>W<sub>2-x</sub>S<sub>2</sub>,

Cr<sub>2</sub>Ge<sub>2</sub>Te<sub>6</sub> and so on).<sup>13, 14, 25, 26</sup> Previous studies have shown that elemental composition plays an important role in determining the physical properties of 2D materials. For example, the typical single-element 2D material graphene has charge carrier mobility but no band gap. Another new single-element 2D material antimonene becomes a semiconductor when it is thinned to a single layer. However, the number of elementary 2D materials is rather limited.

In contrast, binary systems exhibit a relatively diversiform behavior because of their large number of compounds. Good candidates can be easily identified for diverse applications. For example, the indirect band gap can be transformed into a direct band gap by layering the samples. The 1T-2H phase transition

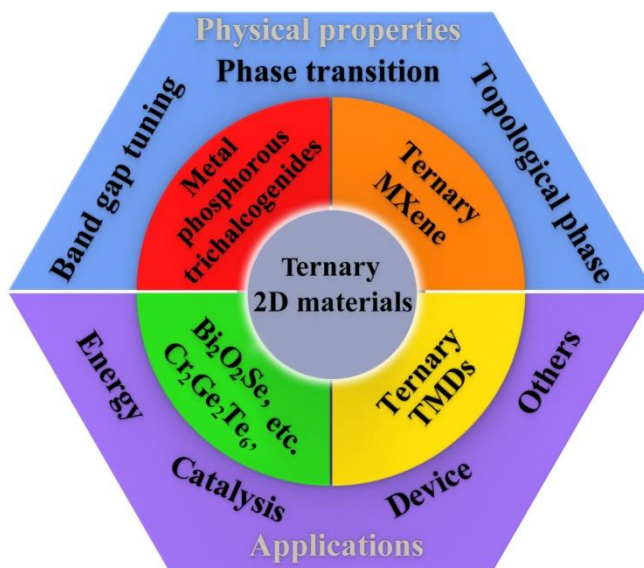


**Figure 1** Schematic representation summarizing the classification, physical properties and applications for ternary 2D materials.

in transition metal dichalcogenides (such as MoTe<sub>2</sub>) can be controlled by the growth temperature. Binary 2D materials exhibit excellent flexibility for tuning the properties through

stoichiometry engineering.<sup>27-30</sup> However, it is difficult to tune the band gap in most binary 2D materials.<sup>31, 32</sup> More importantly, the band gaps of these 2D materials are usually too large to make appropriate optical devices. Although binary InSe was reported to have a relative narrow band gap of 1.4 eV,<sup>33</sup> its application to the near infrared (NIR) range is difficult. However, some TMDs, which have a very narrow band gap might be very good for NIR detectors. In this case, a ternary 2D system may provide a solution to the above mentioned problems.<sup>25, 34</sup> Further, bulk ternary tritellurides CrATe<sub>3</sub> (A = Si, Ge) were predicted to have a small band gap of 0.04 and 0.06 eV, respectively.<sup>35</sup> In copper-indium-selenium systems, the band gap energies of CuIn<sub>3</sub>Se<sub>5</sub> (1.17 eV) and CuIn<sub>5</sub>Se<sub>8</sub> (1.22–1.24 eV) are larger than those of chalcopyrite-type CuInSe<sub>2</sub> (0.99 eV). Importantly, they exhibit a variety of structures depending on the ratio of Cu, In and Se, including chalcopyrite, stannite and wurtzite structures. The crystal structure of the samples changed from chalcopyrite-type CuInSe<sub>2</sub> to hexagonal CuIn<sub>5</sub>Se<sub>8</sub> through stannite-type CuIn<sub>3</sub>Se<sub>5</sub> with increasing x (decreasing Cu/In ratio).<sup>34</sup>

Similar to the ternary copper indium selenide system, ternary 2D systems have multiple degrees of freedom for tailoring physical properties via stoichiometric variation.<sup>23</sup> Further, the ternary system exhibits some properties that are not shown in binary 2D systems. For example, binary 2D materials include metals and semiconductors with exceptionally strong light-matter coupling,<sup>36</sup> charge density wave and superconducting order.<sup>37-40</sup> One strategy to search theoretically for magnetism in 2D materials is to explore the magnetic properties of the single layers exfoliated from a bulk material that exhibits a robust magnetic order.<sup>41</sup> As such, the layered ternary 2D system is an ideal platform for this line of research. MnPX<sub>3</sub> ternary chalcogenides are predicted to have strain-tuneable ferromagnetic phases.<sup>26, 42-44</sup> For larger atomic number compounds such as CrGeTe<sub>3</sub> and CrSnTe<sub>3</sub>, the density functional theory (DFT) predicts ferromagnetic semiconducting phases with Curie temperatures of 80-170 K.<sup>26, 45</sup> The CrGeTe system is a particularly interesting material since it is in a highly rare class of ferromagnetic semiconductors and possesses a layered structure because of the Van der Waals bonds. The Van der Waals bonds make it a candidate 2D atomic crystal, which is predicted as a platform for the study of 2D semiconducting ferromagnets and for single-layered spintronics devices. Spin-phonon coupling can be a key factor for spin relaxation in spintronics devices. Such coupling has also been confirmed in CrGeTe system.<sup>46</sup>

Ternary 2D systems not only exhibit outstanding physical, chemical and electronic properties but also have additional unique properties that binary 2D systems do not possess. In this case, the investigation of ternary 2D systems is of great significance. Figure 1 summarizes the classification, physical properties and potential applications of ternary 2D materials. In this review, the synthesis of ternary TMDs, MPTs, ternary MXenes and other ternary 2D materials is systematically summarized in Section 2, including chemical vapor deposition (CVD), chemical vapor transport (CVT) and molecular beam epitaxy (MBE). In the third section, the structure and characterization of these ternary 2D materials are introduced.

Then, the physical properties, including band gap tuning, phase transition and the topological phase are discussed in Section 4. Furthermore, the potential applications, such as in energy, catalysis and devices are presented. The last section presents the future prospects and a summary of the review.

## 2 Synthesis

### 2.1 Ternary TMDs

Researchers have confirmed that, compared to BCN, some representative ternary TMDs have no phase separation. Moreover, such ternary TMDs have been predicted to be relatively stable owing to their low mixing free energy.<sup>47</sup> CVD is one of the most commonly used methods to obtain ternary TMDs. Shifa *et al.* devised a rational method to synthesize pure ternary Co<sub>x</sub>W<sub>(1-x)</sub>S<sub>2</sub> nanosheets by transferring Co from CoO/carbon fiber (CF) nanowires to the already formed WS<sub>2</sub>/W foil nanosheets. In this experiment, for the first time, Co was incorporated into a WS<sub>2</sub> nanosheet without any concomitant side phases.<sup>48</sup> Another work reported, for the first time, a one-step CVD strategy for the growth of high-quality ternary alloy Mo<sub>(1-x)</sub>W<sub>x</sub>S<sub>2</sub> monolayers on SiO<sub>2</sub>/Si substrates with controllable composition. The Mo<sub>(1-x)</sub>W<sub>x</sub>S<sub>2</sub> and MoS<sub>2</sub>(1-x)Se<sub>2x</sub> alloys, both with excellent uniformity and controllable compositions, were synthesized in this study.<sup>51</sup>

In another work, a single-crystal monolayer Mo<sub>x</sub>W<sub>1-x</sub>S<sub>2</sub> alloy heterostructure with an in-plane inhomogeneous composition was fabricated using the conventional CVD method.<sup>52</sup> Gong *et al.* reported a one-step direct synthesis of MoS<sub>2</sub>(1-x)Se<sub>2x</sub> atomic mono- and bilayers with a broad range of selenium concentrations on SiO<sub>2</sub> by CVD (Figure 2a).<sup>49</sup>

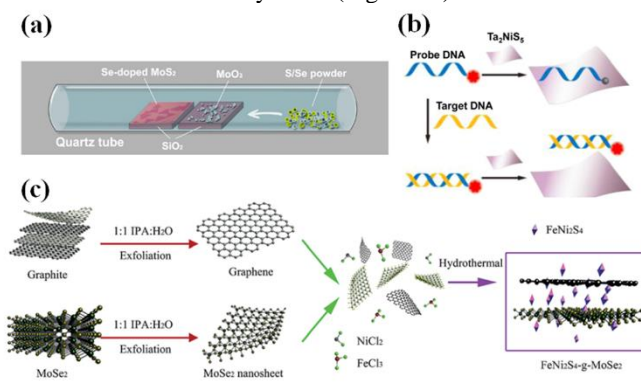


**Figure 2** Methods for preparing ternary TMDs. (a) Controlled synthesis of MoS<sub>2</sub>(1-x)Se<sub>2x</sub> layers via CVD with S/Se powder positioned in the low temperature zone as the source of chalcogens and MoO<sub>3</sub> located at the center of the tube as the Mo source; (b) Schematic illustration of the DNA detection based on single-layer Ta<sub>2</sub>NiS<sub>5</sub> nanosheets; (c) Typical process for the preparation of a FeNiS<sub>4</sub>-graphene-MoSe<sub>2</sub> nanocomposite. Reprinted from Ref 23, 49 with permission from the American Chemistry Society and Ref 50 with permission from the Royal Society of Chemistry.

Another method of preparing ternary TMDs is the CVT approach. For instance, WS<sub>2</sub>(1-x)Se<sub>2x</sub> (x=0.5) crystals have been synthesized by using the CVT method.<sup>53</sup> Konkena *et al.* produced MoSSe@r-GO composite materials, in which MoSSe was synthesized by CVT, followed by a liquid exfoliation process.<sup>54</sup> In addition, ZrS<sub>x</sub>Se<sub>2-x</sub>, which is layered n-type TMD

semiconductor with an indirect band gap, has been obtained by this method.<sup>55</sup> Further, a new ternary phase ZrSTe in the form of a single crystal has been successfully grown from pure elements by using the CVT technique with iodine as the transport agent.<sup>56</sup>

Ternary TMDs can be obtained easily by exfoliation, including mechanical and electrochemical exfoliation. Łapińska reported the Raman measurements of PbSnS<sub>2</sub> thin films obtained by the mechanical exfoliation of a single crystal.<sup>57</sup> Yu *et al.* studied the WSe<sub>2(1-x)</sub>Te<sub>x</sub> monolayer mechanically exfoliated from the bulk by using the CVT method.<sup>58</sup> Tan *et al.* reported the high-yield and scalable preparation of ultrathin 2D TMDs nanosheets, including Ta<sub>2</sub>NiS<sub>5</sub> and Ta<sub>2</sub>NiSe<sub>5</sub>, in solution via electrochemical Li-intercalation and exfoliation of the layered microflakes. The size of the prepared Ta<sub>2</sub>NiS<sub>5</sub> and Ta<sub>2</sub>NiSe<sub>5</sub> nanosheets ranges from tens of nanometers to few micrometers (Figure 2b).<sup>23</sup>

Efforts have been made to find alternative methods of obtaining ternary TMDs. Moreover, PLD, solid-state reactions and hydrothermal methods have been proven to be effective approaches for preparing ternary TMDs. Considering the relatively high growth temperature required for CVD growth that promotes the formation of defects, Yao *et al.* proposed the growth of large-scale and high-quality Mo<sub>0.5</sub>W<sub>0.5</sub>S<sub>2</sub> alloy films via PLD.<sup>61</sup> Moreover, MoS<sub>2(1-x)</sub>Se<sub>2x</sub> is obtained using a high-temperature solid-state reaction technique. Typically, MoS<sub>2(1-x)</sub>Se<sub>2x</sub> crystals are obtained by heating a mixture of the constituent elements in the required atomic ratio in an

× 3.0 mm in size were obtained by using the CVT method with iodine as the transport agent. In this process, stoichiometric amounts of the Mn, P and S powders were used as the reactant, and the reaction was carried out for 120 h in a two-zone electric furnace.<sup>66</sup> Du *et al.* synthesized and exfoliated the bulk crystals of MPS<sub>3</sub> (M = Fe, Mn, Ni, Cd, Zn) sulphides and MPSe<sub>3</sub> (M = Fe and Mn) selenides in MPTs, using the CVT and mechanical exfoliation methods, respectively (Figure 3a).<sup>59</sup> In fact, the CVT strategy is also applied to prepare other types of MPTs, such as CoPS<sub>3</sub> and SnPS<sub>3</sub>.<sup>67</sup> Note that, in some cases, such as in the synthesis of layered FePS<sub>3</sub> and MnPS<sub>3</sub>, the CVT method is called a solid-state reaction.<sup>68, 69</sup> Typically, the conventional CVT process requires a long reaction time, making it inconvenient for practical purposes. In light of this situation, Villanueva *et al.* presented a microwave-assisted preparation of MPS<sub>3</sub> materials (M = Mn, Cd), which shortened the reaction time dramatically, allowing an efficient and rapid synthesis of MPS<sub>3</sub> materials (Figure 3b).<sup>60</sup>

Additional methods have also been used to obtain MPTs, such as the solvent exfoliation and ion-exchange solvothermal methods. In one case, few-layer FePS<sub>3</sub> were obtained using solvent exfoliation developed by Mukherjee *et al.*<sup>70</sup> Furthermore, a polycrystalline nanoparticle sample of MnPS<sub>3</sub> was prepared via the ion-exchange solvothermal method.<sup>74, 75</sup>

### 2.3 Ternary MXenes

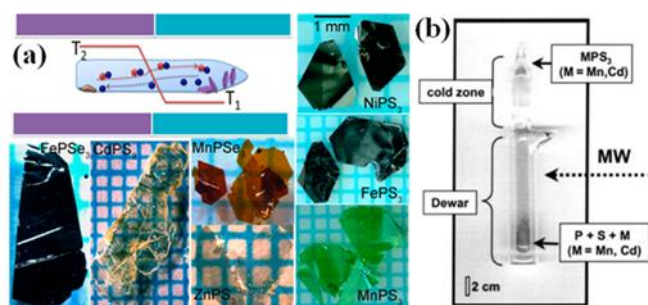


**Figure 3** Methods for preparing MPTs. (a) CVT method and photos of bulk 2D crystals. They are put on the coordinate paper, in which the smallest square is 1 mm × 1 mm; (b) A picture of the Dewar ampoule highlighting its different parts and the process of MPS<sub>3</sub> crystallization. Reprinted from ref. 59 with permission from the American Chemistry Society and ref. 60 with permission from Wiley.

evacuated quartz tube at 800 °C for three days.<sup>62</sup> Further, Shen *et al.* designed FeNi<sub>2</sub>S<sub>4</sub>-graphene-MoS<sub>2</sub> and FeNi<sub>2</sub>S<sub>4</sub>-graphene-MoSe<sub>2</sub> composites with an in situ hydrothermal method (Figure 2c).<sup>50, 63</sup>

### 2.2 MPTs

The most commonly adopted method of synthesizing MPTs is CVT, which exhibits a high conversion rate of raw materials. Single-crystal FePS<sub>3</sub> was grown using this method by Lee *et al.*<sup>64</sup> and Wang *et al.*<sup>65</sup> using pure Fe, P, and S powders. In addition, large single-crystal MnPS<sub>3</sub> samples approximately 3.0

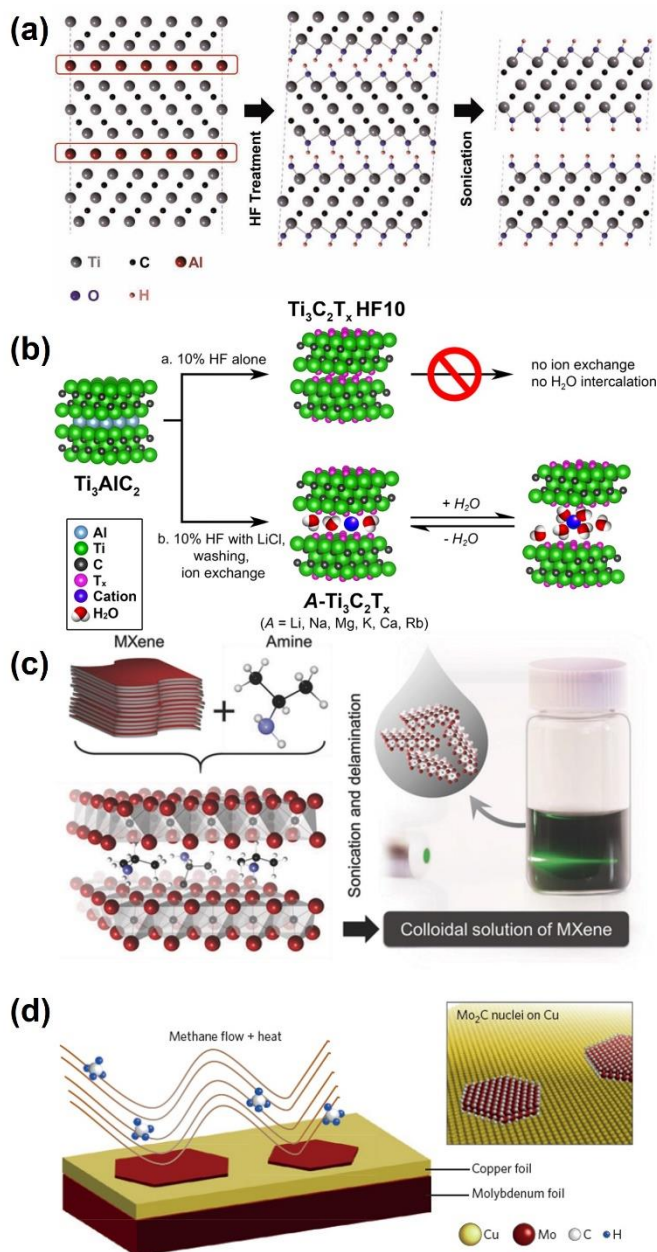


**Figure 4** Methods for preparing MXenes. (a) Schematic of the exfoliation process for  $\text{Ti}_3\text{AlC}_2$ ; (b) Pathway of materials prepared in this report; (c) Schematic of  $\text{Nb}_2\text{CT}_x$  delamination process via isopropylamine intercalation; (d) 2D carbide crystals produced by CVD. Reprinted from Ref.13 with permission from the American Chemistry Society; Ref 71 with permission from Nature Publishing Group and Ref 72, 73 with permission from Wiley.

MXenes, a new and potentially very large group, are first synthesized by selectively etching out certain “A” layers from the MAX phases at room temperature (Figure 4a).<sup>72</sup> The composition of MAX can be expressed as  $\text{M}_n\text{AX}_{n-1}$ , where M denotes an early transition metal, A is mainly a group IIIA or IVA element, X is C and/or N, and  $n = 2-4$ . As noted, in 2011,  $\text{Ti}_3\text{C}_2$ , was first synthesized by selectively etching the Al atoms in  $\text{Ti}_3\text{AlC}_2$ , using aqueous hydrofluoric acid (HF) at room

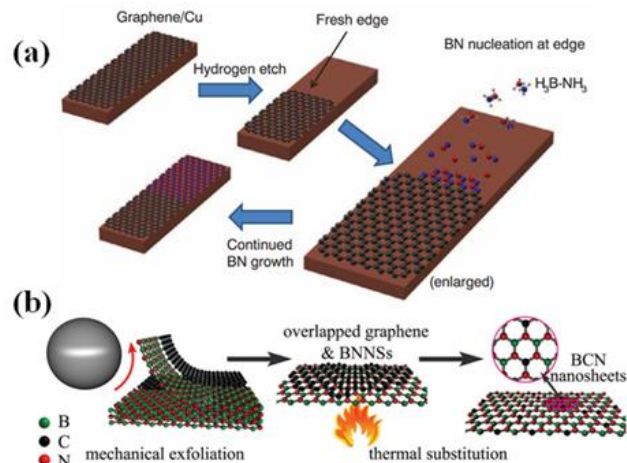
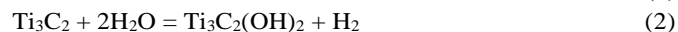
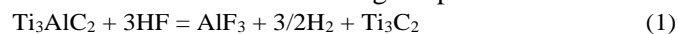


**Figure 5** Methods for preparing BCN. (a) Cartoon illustration of epitaxial growth of BN onto graphene edges; (b) Schematic of the processing steps involved in the synthesis of BCN nanosheets. Reprinted from Ref 81 with permission from Science and Ref 82 with permission from the Royal Society of Chemistry.

temperature.<sup>72</sup> The process of  $\text{Ti}_3\text{AlC}_2$  etching with HF can be summarized as the following simplified reactions:



Reaction (1) is essential and is followed by Reaction (2) and/or (3). Note that by adjusting the etching time and the concentration of HF, numerous MXenes can be synthesized utilizing HF etching from room temperature to 55 °C.<sup>76</sup> Meanwhile, a longer reaction time and stronger etching are required for increasing the atomic numbers of M. This phenomenon may be related to the metallic M-Al bonding,<sup>77</sup> since a larger number of M valence electrons requires stronger etching.<sup>78</sup>

The etching process is dependent on kinetics. Therefore, the required etching time is different for various MXenes.<sup>78</sup> Moreover, a complete dissolution or recrystallization of  $\text{M}_{n+1}\text{X}_n\text{T}_x$  layers may occur under excessive heating.<sup>79, 80</sup>

Except for HF etching, MXenes can also be obtained by using a mixture of a strong acid and a fluoride salt. Ghidui *et al.* reported a synthesis route to multi-layered  $\text{Ti}_3\text{C}_2\text{T}_x$  by immersing  $\text{Ti}_3\text{AlC}_2$  in a milder etchant solution composed of hydrochloric acid (HCl) and lithium fluoride (LiF) (Figure 4b).<sup>83-85</sup> The reaction between HCl and LiF can produce HF, which selectively etches the Al atoms. During the etching process via metal halide, the MXene layers are intercalated by the cations and water molecules, leading to increased interlayer spacing. Compared with pure HF etching, this method can produce single- or few-layer flakes with high efficiency. For example, Lipatov *et al.* demonstrated an improved method of LiF-HCl selective etching of  $\text{Ti}_3\text{AlC}_2$ , which yields large, high-quality monolayer  $\text{Ti}_3\text{C}_2\text{T}_x$  MXene flakes with well-defined and clean edges and visually defect-free surfaces.<sup>86</sup>

To further investigate the 2D properties of the as-prepared multi-layered MXenes, it is imperative and indispensable to obtain single- or few-layer compounds in the production. One effective method to achieve exfoliation is the intercalation of polar organic molecules into the interlayers of MXenes. When

DMSO was intercalated into  $Ti_3C_2$  and then sonicated in water,  $Ti_3C_2$  delaminated, forming a stable colloidal solution that was filtered to produce MXene ‘paper’.<sup>87</sup> In another case, DMSO was replaced by amine to delaminate the second representative of the MXene family-Nb<sub>2</sub>CT<sub>x</sub> (Figure 4c).<sup>73</sup> Naguib *et al.* reported a general approach for the large-scale delamination of MXenes by using a relatively large molecular organic base, namely tetrabutylammonium hydroxide (TBAOH), choline hydroxide, or n-butylamine.<sup>88</sup>

Alternative MXenes preparation methods have also been explored and chemical vapor deposition (CVD) was proven to be feasible (Figure 4d).<sup>89</sup> The MXenes prepared by this method have the characteristics of a large lateral dimension and few defects. However, the detailed experimental conditions need to be explored further.

#### 2.4 BCN and other types of ternary 2D materials

BCN is a representative ternary 2D system that was explored prior to the discovery of graphene.<sup>90, 91</sup> However, the main obstacle, phase separation, hinders the homogenous synthesis of this material.<sup>47</sup> Although numerous works have been conducted and methods proposed to obtain h-BCN, obtaining the ‘real’ BCN without phase separation remains a challenge. The methods of preparing BCN are found to be diverse, among which the CVD is the most commonly adopted method. Indeed, by providing the B, C and N sources, the BCN layer can be synthesized.<sup>22, 92</sup> A catalyst-free CVD synthesis of BCN nanosheets with a tunable B and N bond structure by thermally decomposing solid urea, boric acid and polyethylene glycol (PEG) precursors was developed.<sup>93</sup> Liu *et al.* demonstrated the epitaxial growth of a single-atomic-layer, in-plane heterostructure of graphene and hexagonal boron nitride (h-BN) by atmospheric-pressure CVD. Interestingly, in this case, the h-BN lattice orientation is only determined by the graphene (Figure 5a).<sup>81</sup> Gong’s group have demonstrated a direct chemical conversion of graphene to high-quality BCN with a full range of compositions, which systematically converts conducting graphene into semiconducting ternary h-BCN.<sup>94</sup> This strategy makes it possible to produce uniform BCN structures without disrupting the structural integrity of the original graphene templates.<sup>91, 94</sup>

Pulsed laser deposition (PLD), a facile and efficient technique for growing high quality thin films, can control the structure and composition of the as-prepared film. Moreover, compared with CVD, the flammable gas hydrogen is not required for the PLD method. Amorphous BCN films were synthesized by PLD under various laser fluences. The bonding structure of the as-prepared films changed according to the laser fluences.<sup>37</sup> In another work, Zhang *et al.* fabricated BCN films with large carbon stoichiometric range using PLD with BN-N sources.<sup>95</sup> Huang *et al.* developed a facile carbon-doping pyrolysis synthesis method to produce BCN nanosheets. In brief, the mixture containing glucose, boron oxide and urea was put into a tube furnace in an ammonia atmosphere for 5 h at 1250 °C.<sup>96</sup> Bulk BCN spheres were deposited on the substrate via an organic precursor pyrolysis method. Moreover, BCN materials

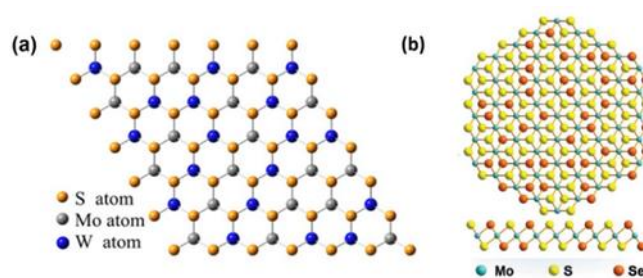


**Figure 6** (a) Structure of  $Mo_{1-x}W_xS_2$  ( $x=0.5$ ). Reprinted from Ref. 102 with permission from the American Chemistry Society. (b) Structure of  $MoS_{2x}Se_{2(1-x)}$ . Reprinted from Ref. 103 with permission from Wiley.

with a tunable structure, including microspheres and nanoflakes were obtained by controlling the heat treatment of BCN organic precursor pyrolysis.<sup>97, 98</sup> Recently, the in-vacuum thermolysis of a single-source precursor, ethane 1,2-diamineborane ( $BH_3NH_2CH_2CH_2NH_2BH_3$ ), was performed to form bulk ternary BCN. The authors aimed to reduce the presence of oxides at the BCN surface, an essential issue linked to many potential applications of BCN materials.<sup>99</sup>

Ma *et al.* proposed a ‘thermal substitution’ method for preparing BCN nanosheets through substitutional C doping of h-BN nanosheets (Figure 5b). In comparison to the existing synthesis methods, it has several advantages, such as milder reaction conditions and higher yield. Owing to the adjustable C content of the BCN, a tuned band gap was achieved.<sup>82, 98</sup>

Many attempts were made to explore other methods of obtaining BCN, including magnetron sputtering<sup>100</sup> and ion beam-assisted deposition (IBAD).<sup>101</sup> For example, well-adherent BCN thin films with different compositions were grown by the reactive DC magnetron sputtering of a B<sub>4</sub>C target with different nitrogen flows.<sup>104</sup> A further example is the deposition of BCN coatings with controlled atomic compositions using the IBAD technique with composite C/B targets.<sup>101</sup>

Beniwal *et al.* utilized thermally induced dehydrogenation of the  $B_2N_2C_2H_{12}$  precursor molecules and formed an epitaxial BCN monolayer on Ir (111) through covalent bond formation. In this experiment, atomically flat Ir substrates were exposed under ultrahigh vacuum to bis-BN cyclohexane vapor.<sup>105</sup>

In addition to the materials mentioned above, other types of ternary 2D materials, such as  $Bi_2O_2Se$ <sup>106</sup> and  $Cr_{1-x}Ge_xTe$ , have been reported.<sup>46</sup> Recently, Peng *et al.* reported ultrathin films of non-encapsulated layered  $Bi_2O_2Se$ ,<sup>106</sup> grown by a home-made low-pressure CVD system, which demonstrate excellent air stability and high-mobility semiconducting behavior. A hall mobility value of more than 20,000  $cm^2 V^{-1} s^{-1}$  was measured in as-grown  $Bi_2O_2Se$  nanoflakes at low temperatures.  $Bi_2O_3$  powder and  $Bi_2Se_3$  bulk were the source materials. The ultrahigh mobility characteristics of  $Bi_2O_2Se$  may be more generally applicable to other ternary members ( $Bi_2O_2S$  and  $Bi_2O_2Te$ ) with tunable band gaps. In 2016, Fukuma *et al.* synthesized IV–VI diluted magnetic semiconductor  $Ge_{1-x}Cr_xTe$  epilayers on  $SrF_2$  substrates by using the MBE method.<sup>46</sup> The Cr composition increased up to  $x = 0.1$ , compared with that of  $x = 0.06$  on the  $BaF_2$  substrates. The Curie temperature increased with an increase in the

Cr composition, and a relatively high value of 200 K was realized in

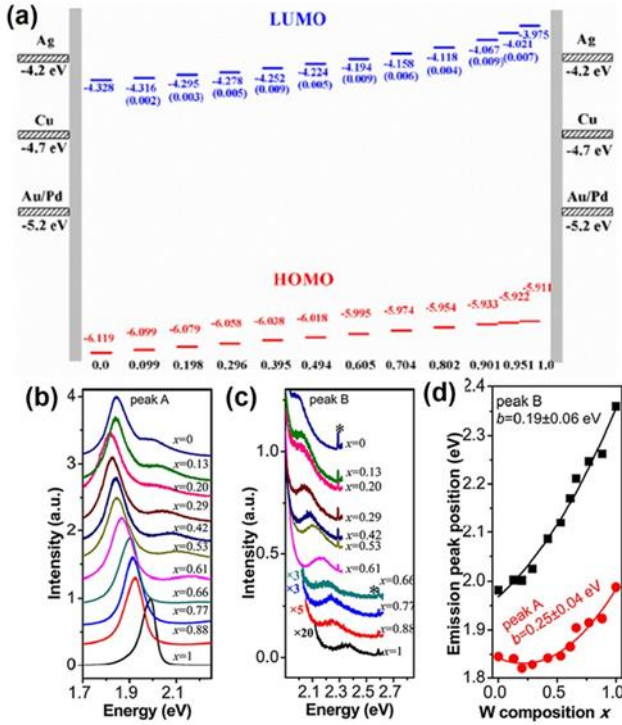


**Figure 7** (a) The absolute energy level of HOMO and LUMO for  $\text{Mo}_{1-x}\text{W}_x\text{S}_2$  monolayer alloys as a function of W composition  $x$ . The number in the bracket is the error bar of the LUMO energy. The frontier orbital energies are compared to the Fermi levels of four metal electrode materials: Au, Ag, Cu and Pd. Reprinted from Ref. 110 with permission from the American Chemistry Society. (b-d) Composition-dependent PL emission from  $\text{Mo}_{1-x}\text{W}_x\text{S}_2$  monolayers. (b,c) PL spectra of  $\text{Mo}_{1-x}\text{W}_x\text{S}_2$  monolayers with different W compositions  $x$ . The PL intensity is normalized by the maximum emission intensity. The spectra were excited by 514.5 nm for  $x = 0 - 0.61$  and 457.9 nm for  $x = 0.66 - 1$ . The peaks marked by \* are Raman peaks of Si substrates. (d) Composition-dependent emission energies for A and B excitons. The red and black lines are parabola fittings for composition-dependent energy of peaks A and B. Reprinted from Ref. 102 with permission from the American Chemistry Society.

the diluted magnetic semiconductors.

### 3 Structure, characterization and properties

#### 3.1 Ternary TMDs

Compared with binary TMDs, ternary TMDs enable the control of local electronic structures and provide flexibility to fine tune the specific properties and applications by adding a third element to the structure.<sup>47, 58, 62, 102, 103, 107-109</sup> Ternary TMDs have a general formula of  $\text{M}'_a\text{M}''_{(1-a)}\text{X}_2$  ( $\text{M}'$  and  $\text{M}''$  are two different transition metals;  $\text{X} = \text{S}, \text{Se}$  or  $\text{Te}$ ;  $a = 0$  to 1) or  $\text{M}'X'_2aX''_{2(1-a)}$  ( $\text{M}$  = transition metals;  $\text{X}' = \text{S}, \text{Se}, \text{Te}$ ;  $\text{X}'' = \text{S}, \text{Se}, \text{Te}$ ;  $\text{X}' \neq \text{X}''$ ;  $a = 0$  to 1).

The structure of  $\text{MX}_2$  ( $\text{M} = \text{Mo}, \text{W}$ ;  $\text{X} = \text{S}, \text{Se}$ ) is shown in Figure 6. In  $\text{MoS}_2$ , each Mo center occupies a trigonal coordination sphere that is bound to six S atoms. Each S atoms is connected to three Mo centers. In ternary TMD  $\text{Mo}_{1-x}\text{W}_x\text{S}_2$  and

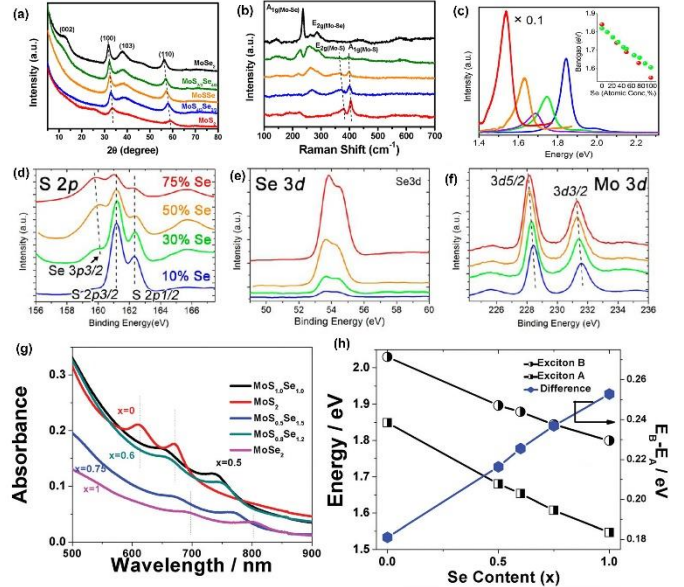


**Figure 8** (a) XRD characterizations of  $\text{MoS}_2x\text{Se}_2(1-x)$ . (b) Raman characterizations of  $\text{MoS}_2x\text{Se}_2(1-x)$ . (a-b) Reprinted from Ref. 108 with permission from the American Chemistry Society. (c) PL spectra of pristine  $\text{MoS}_2$  (blue),  $\text{MoS}_{1.4}\text{Se}_{0.6}$  (green),  $\text{MoS}_1\text{Se}_1$  (purple),  $\text{MoS}_{0.5}\text{Se}_{1.5}$  (orange), and  $\text{MoSe}_2$  (red), respectively, measured with a 488 nm laser. Inset: red dots, the Se concentration dependency of the PL optical gap of  $\text{MoS}_2x\text{Se}_2(1-x)$  showing a linear decrease from  $\sim 1.85$  eV (pure  $\text{MoS}_2$ ) to  $\sim 1.54$  eV (pure  $\text{MoSe}_2$ ). (d-f) XPS spectra of S 2p, Se 3d, and Mo 3d core levels in the monolayer  $\text{MoS}_2x\text{Se}_2(1-x)$  with different Se concentration ( $x = 0.1, 0.3, 0.50, \text{ and } 0.75$ ). (c-f) Reprinted from Ref. 49 with permission from the American Chemistry Society. (g) Absorbance spectra of  $\text{MoS}_2x\text{Se}_2(1-x)$  with varying  $x$  and (h) shows energies of excitons A, B and energy difference of excitons A and B as a function of Se content. (g-h) Reprinted from Ref. 62 with permission from the Royal Society of Chemistry.

$\text{MoS}_2x\text{Se}_2(1-x)$ , the Mo or S atoms are replaced by the W or Se atoms with different mole ratios.

Xi *et al*<sup>110</sup> calculated the composition-dependent electronic properties of  $\text{Mo}_{1-x}\text{W}_x\text{S}_2$  by using first-principles calculations. The absolute levels of HOMO and LUMO in  $\text{Mo}_{1-x}\text{W}_x\text{S}_2$  were determined by vacuum level calibration (Figure 7a). As the number of W atoms increases, the HOMO level rises linearly and the LUMO level exhibits an energy bowing, which further lead to the band gap bowing effect in  $\text{Mo}_{1-x}\text{W}_x\text{S}_2$ . The experimental band gap changes was observed using PL measurement by Chen *et al.*<sup>102</sup> As the W composition  $x$  increases, the A exciton emission red-shifts and then blue-shifts (Figure 7b). In contrast, the B exciton emission blue-shifts continuously (Figure 7c). The exciton emission can be tuned from 1.82 to 1.99 eV, whereas the B exciton emission can be tuned from 1.98 to 2.36 eV. The bowing effect can also be seen from the PL measurement. By fitting the experimental data, we can obtain the bowing parameter of  $0.25 \pm 0.04$  eV and  $0.19 \pm 0.06$  eV for A exciton emission and B exciton emission, respectively (Figure 7d). With increasing selenium content in  $\text{MoS}_2x\text{Se}_2(1-x)$ ,<sup>49, 62, 108</sup> all main diffraction peaks are downshifted continuously (Figure 8a). Because of the gradual expansion of unit cells upon the substitution of sulphur atoms

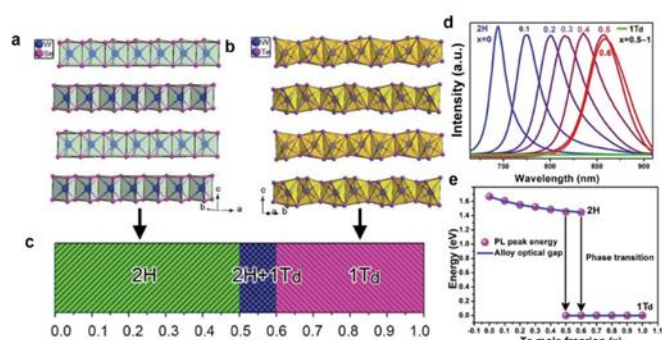


**Figure 9** (a) The crystal structure of 2H WSe<sub>2</sub>. (b) The crystal structure of 1Td WTe<sub>2</sub>. (c) Different phases with dependence of concentration  $x$  in WSe<sub>2(1-x)</sub>Te<sub>2x</sub>. (d) The PL spectrum of the composition monolayer 2H WSe<sub>2(1-x)</sub>Te<sub>2x</sub> ( $x = 0-0.6$ ) alloys. (e) Composition dependent ( $x$ ) band gaps of the monolayer WSe<sub>2(1-x)</sub>Te<sub>2x</sub> ( $x = 0-0.6$ ) alloys. Reprinted from Ref. 58 with permission from Wiley.

with larger selenium atoms, the (100) and (110) peaks are downshifted, which implies their mixing at the atomic level. Furthermore, the (103) peak intensity becomes more heightened. From the Raman spectra (Figure 8b) under 514-nm laser excitation, two sets of composition-dependent vibration modes can be observed: Mo-Se related modes at low frequency (200-300 cm<sup>-1</sup>) and Mo-S related modes at high frequency (350-410 cm<sup>-1</sup>), which belong to the typical MoS<sub>2x</sub>Se<sub>2(1-x)</sub> alloy.<sup>111, 112</sup> With the introduction of selenium, the two vibration modes (E<sub>2g</sub> at 381 cm<sup>-1</sup> and A<sub>1g</sub> at 403 cm<sup>-1</sup>) shift to a lower frequency. Simultaneously, Mo-Se related modes (E<sub>2g</sub> at 285 cm<sup>-1</sup> and A<sub>1g</sub> at 236 cm<sup>-1</sup>) start to gain increasing intensity. The PL measurements (Figure 8c) confirmed the optical band gap change from 1.85 to 1.54 eV with the increasing selenium content. The optical band gap was linearly dependent on the Se concentration in MoS<sub>2x</sub>Se<sub>2(1-x)</sub>. This linear dependence was also confirmed by Kiran *et al* (Figure 8h).<sup>62</sup> From the XPS results (Figures 8d-f), with increasing Se concentration, the intensity of the S 2p peaks (~162.3 and 161.2 eV) decreases, whereas peaks from Se 3p<sub>3/2</sub> (~159.8 eV) and Se 3d (~54 eV, Figure 8e) appear and become dominant.

Yu *et al*<sup>58</sup> reported that phase transition from 2H to the 1Td structure occurred in WSe<sub>2(1-x)</sub>Te<sub>2x</sub>. The crystal structure of 2H WSe<sub>2(1-x)</sub>Te<sub>2x</sub> was similar to that of 2H MoS<sub>2</sub>, which showed WSe<sub>6</sub> or WSe/Te<sub>6</sub> triangular prism layers bonded together (Figure 9a). In contrast, in the 1Td WSe<sub>2(1-x)</sub>Te<sub>2x</sub> structure, the WTe<sub>6</sub> or WSe/Te<sub>6</sub> octahedra were linked with each other by sharing the Te-Te edges (Figure 9b). By tuning the concentration of Te from 0% to 100%, 2H WSe<sub>2(1-x)</sub>Te<sub>2x</sub> was obtained at  $x = 0-0.4$ , while 1Td WSe<sub>2(1-x)</sub>Te<sub>2x</sub> was obtained at  $x = 0.7-1.0$ . Interestingly, at  $x = 0.5$  to 0.6, an intermediate state appears with two phases (1Td and 2H) (Figure 9c). The phase transition is confirmed by the PL spectra of the monolayer samples excited with a 532-nm laser. The PL peak continuously shifts from 744 nm to 857 nm (near infrared). No PL signal is detected when  $x \geq 0.6$  for the 1Td samples (Figure 9d). In Figure 9e, the band gaps are shifted continuously from 1.67 eV to 1.44 eV. Furthermore, the optical gap directly changes from 1.44 to 0 eV when  $x \geq 0.6$ . This indicates that

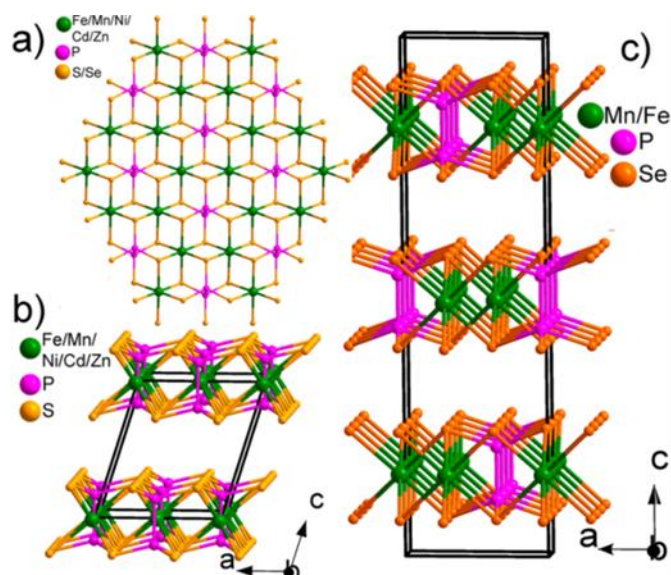


**Figure 10** (a) Arrangement of metal, phosphorus and sulfur or selenium atoms in the plane of MPS<sub>3</sub> (M = Fe, Mn, Ni, Zn and Cd) and MPSe<sub>3</sub> (M = Fe and Mn); (b) packing structure of MPS<sub>3</sub>; (c) packing structure of MPSe<sub>3</sub>. Reprinted from Ref. 59 with permission from the American Chemistry Society.

**Table 1** Band gap of selected bulk APX<sub>3</sub>.<sup>59, 119</sup>

Compound	Band gap (eV)
FePS <sub>3</sub>	1.5
MnPS <sub>3</sub>	3.0
NiPS <sub>3</sub>	1.6
CdPS <sub>3</sub>	3.5
ZnPS <sub>3</sub>	3.4
FePSe <sub>3</sub>	1.3
MnPSe <sub>3</sub>	2.5

WSe<sub>2(1-x)</sub>Te<sub>2x</sub> alloys undergo a phase transition from semiconductor (2H phase) to metal (1Td phase).

Weyl fermions have been known since the early twentieth century as chiral particles associated with solutions to the Dirac equation at zero mass<sup>113, 114</sup>. There is only one type of Weyl fermion in high-energy physics, but exactly two types of Weyl points (WPs)<sup>115</sup> in condensed matter systems. In type-I Weyl semi-metals, the bulk Fermi surface shrinks to a point at the Weyl node, whereas in type-II Weyl semimetals, the Weyl cone arises as a connector of holes and electron pockets, where the large tilt of the cone induces a finite density of states at the node energy. This fundamental difference can, for instance, cause an anomalous Hall effect in type-II Weyl semimetals. Belopolski *et al*,<sup>115, 116</sup> reported the experimental discovery of the first type-II Weyl semi-metal in Mo<sub>x</sub>W<sub>1-x</sub>Te<sub>2</sub>. Then, it was further predicted that a type-II Weyl semi-metal arises in binary and WTe<sub>2</sub>.<sup>116, 117</sup> Concurrently, MoTe<sub>2</sub> and other ternary TMDs were predicted to be Weyl semi-metals<sup>118</sup>. Koepf *et al*. identified TaIrTe<sub>4</sub> as a new member of this family of Weyl semi-metals.<sup>118</sup> TaIrTe<sub>4</sub> has the attractive feature that it hosts only four well-separated Weyl points, the minimum imposed by symmetry. Moreover, the topological surface states, Fermi arcs

and connecting Weyl nodes of opposite chirality extend to

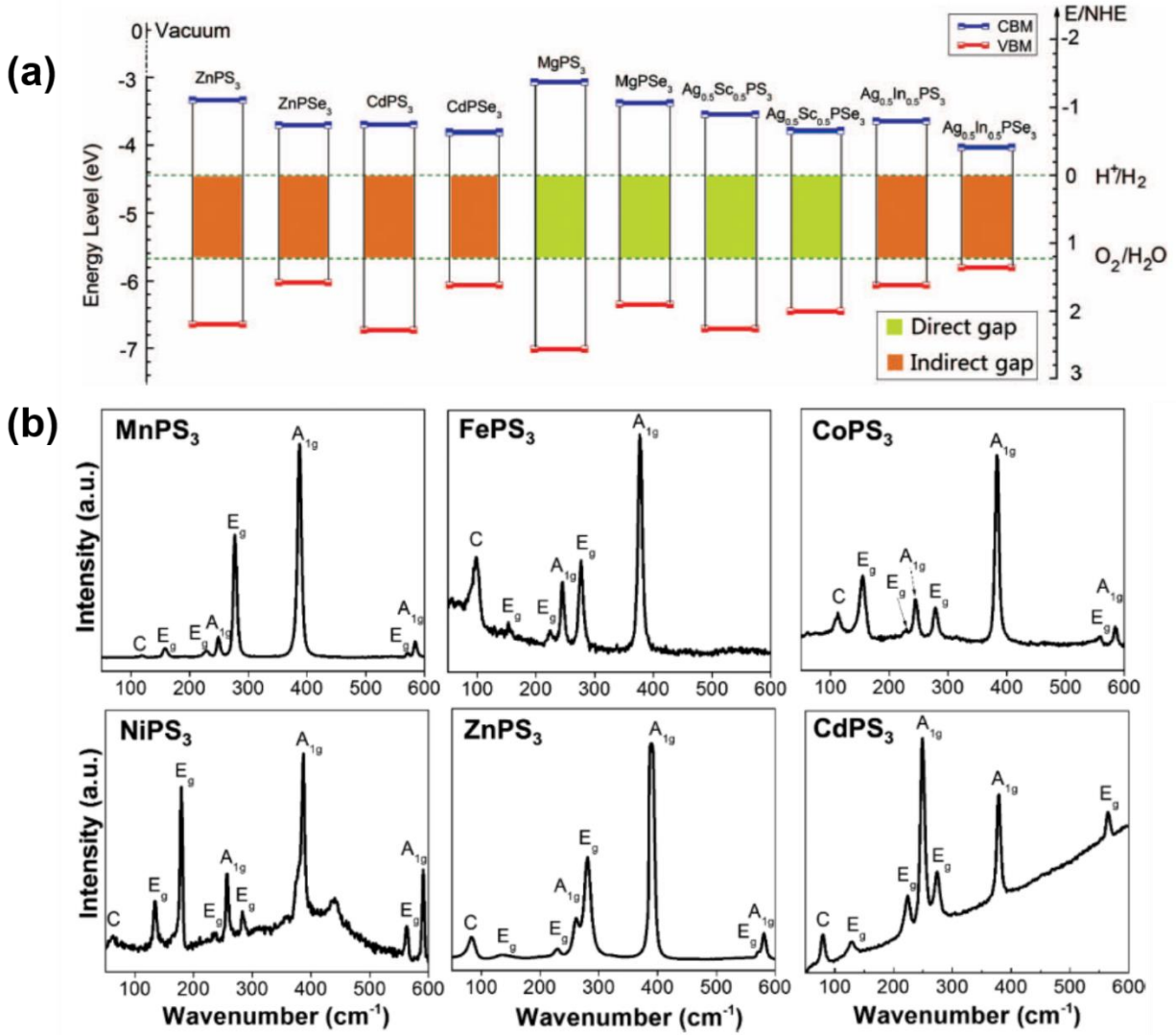


**Figure 11** (a) Band edge positions of single-layer APX<sub>3</sub>. The energy scale is indicated by either the normal hydrogen electrode (NHE) (right Y-axis) or the vacuum level (left Y-axis) in electron volts as a reference. The redox potentials (green dashed line) of water splitting are shown for comparison. Reprinted from Ref. 122 with permission from the AIP Publishing. (b) Raman spectrum of transition metal MPS<sub>3</sub> phases. Reprinted from Ref. 67 with permission from the American Chemistry Society.

approximately 1/3 of the surface Brillouin zone. This large momentum-space separation is highly favourable for detecting the Fermi arcs spectroscopically and in transport experiments. All three telluride compounds show a minimum set of four Weyl points, occurring at very similar positions in the  $k$  space.

### 3.2 MPTs

Metal phosphorus trichalcogenides (MPTs) have been in existence since the 19<sup>th</sup> century, and have not been explored comprehensively on the atomically thin level.<sup>120</sup> Their general formula is M<sup>II</sup>PX<sub>3</sub> (M<sup>II</sup>= Fe, Mn, Zn, Co, Ni, Cd, Mg, etc.; X=S, Se) and M<sup>I</sup>M<sup>III</sup>P<sub>2</sub>X<sub>6</sub> (M<sup>I</sup>= Ag, Cu; M<sup>III</sup>= Cr, V, Al, Ga, In, Bi, etc.). The metal of the MPTs family is mainly from vanadium to zinc, which has more possible compounds than TMDs (IVB, VB and VIB).<sup>121</sup>

In MPX<sub>3</sub> crystals, each unit cell is composed of two cations and one [P<sub>2</sub>X<sub>6</sub>]<sup>4-</sup> cluster. The M atoms are coordinated with six X

atoms, while the P atoms are coordinated with three X atoms and one P atom to form a [P<sub>2</sub>S<sub>6</sub>]<sup>4-</sup> unit, which is arranged as a honeycomb structure (as shown in Figure 10a). The atomic layers of the sulphides stack in the C2/m space group (Figure 10b) while those of the selenide stack in R-3 (Figure 10c). The two cations can be two M<sup>II</sup> or one M<sup>I</sup> with M<sup>III</sup>.

In bulk MPX<sub>3</sub> crystals, due to the changes of the metal and chalcogenide atoms, the band gap can range from 1.3 to 3.5 eV (Table 1), which indicates a wide wavelength optoelectronic response. From DFT calculations,<sup>122</sup> the monolayer metal phosphorus trichalcogenides have very low formation energies and the band gap can vary in a wide range (Figure 11a). Meanwhile, the electronic structures are affected greatly by the

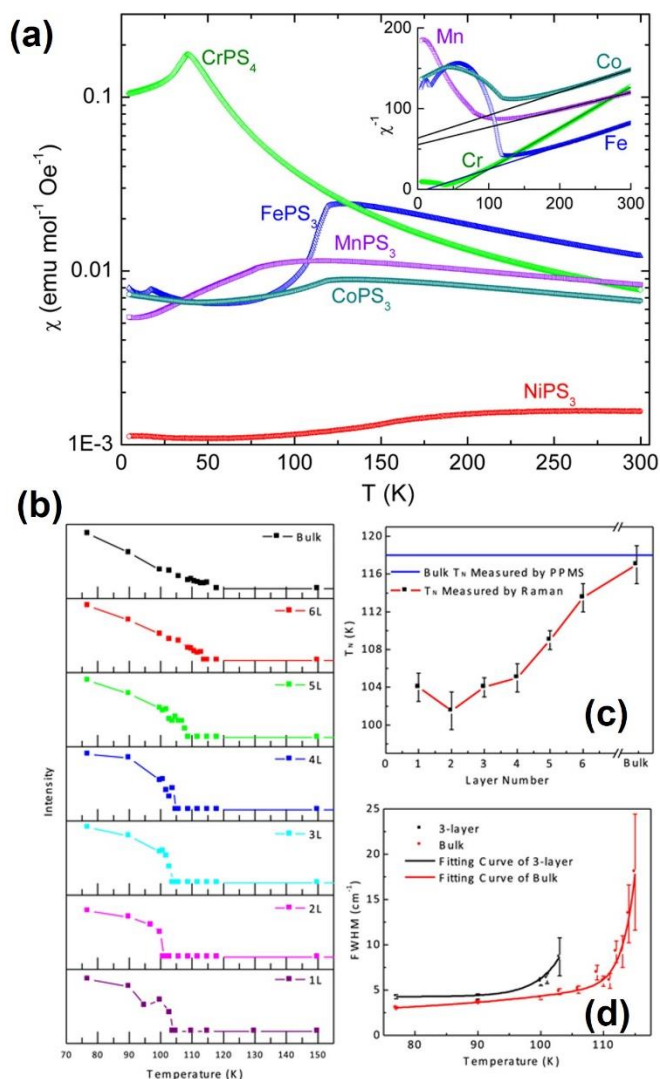


**Figure 12** (a) Magnetic susceptibility of  $\text{MnPS}_3$ ,  $\text{CoPS}_3$ ,  $\text{NiPS}_3$ ,  $\text{FePS}_3$  and  $\text{CrPS}_4$  phases measured at a field of 1000 Oe. The inset is the inverse susceptibility representation (without  $\text{NiPS}_3$ ). Reprinted from Ref. 67 with permission from the American Chemistry Society. (b) Plots of intensity of Raman peak at  $88 \text{ cm}^{-1}$  versus temperature of samples in different thickness. (c) Plot of Néel temperature ( $T_N$ ) measured by optical method versus thickness of samples, compared with the result of bulk sample measured by PPMS. (d) Plots of FWHM of Raman peak at  $88 \text{ cm}^{-1}$  versus temperature of trilayer and bulk samples. Reprinted from Ref. 65 with permission from the IOP Science.

metal or the chalcogenide atoms. It is interesting that for all the listed monolayer  $\text{MPX}_3$  in Figure 11a, the minimum potentials of the conduction bands are higher than the reduction potential of hydrogen, and the maximum potentials of the valence bands are lower than the oxidation potential of  $\text{O}_2/\text{H}_2\text{O}$ . These results indicate that such materials are thermodynamically feasible for both water oxidation and reduction reactions. Furthermore, the strain in monolayer  $\text{MPX}_3$  ( $M = \text{Zn, Cd}$ ;  $X = \text{S, Se}$ ) also affects the band structure and further modulates the electronic structures.<sup>123</sup> Transitions between indirect and direct band gaps

are observed using compressive strain engineering for  $\text{ZnPS}_3$ ,  $\text{ZnPSe}_3$  and  $\text{CdPSe}_3$ , but not for  $\text{CdPS}_3$ .

**Table 2** The Néel temperature of  $\text{MPS}_3$  ( $M = \text{Mn, Fe, Co, Ni}$ ).

Compounds	The Néel temperature ( $T_N$ ) (K)	Method	Reference
$\text{MnPS}_3$ (Bulk)	82	NMR of $^{31}\text{P}$	121
	86	Magnetic Susceptibility	66
	115	Magnetic Susceptibility	67
$\text{FePS}_3$ (Bulk)	120	Magnetic Susceptibility	67
	117	Raman	65
	116	NMR of $^{31}\text{P}$	121
	117.4	Mössbauer spectroscopy	126
$\text{FePS}_3$ (Monolayer)	104	Raman	65
$\text{CoPS}_3$	122	Neutron diffraction	121
	132	Magnetic Susceptibility	67
$\text{NiPS}_3$	155	NMR of $^{31}\text{P}$	121
	265	Magnetic Susceptibility	67

The Raman mode of  $\text{MPS}_3$  ( $M = \text{Mn, Fe, Co, Ni, Zn, Cd}$ ) originates from two parts of the structure. One part is attributed to the  $[\text{P}_2\text{S}_6]^{4-}$  cluster and eight Raman active modes with  $D_{3d}$  symmetry ( $3A_{1g}$  and  $5E_g$  Raman active modes).<sup>67</sup> The  $A_{1g}$  modes can be observed at around  $590, 387$  and  $255 \text{ cm}^{-1}$  and  $E_g$  modes at around  $560, 283, 235, 180$  and  $150 \text{ cm}^{-1}$ . The overtones of the  $A_{1g}$  modes are not observed in all  $\text{MPS}_3$  compounds. In particular, it was found in  $\text{NiPS}_3$  at  $815$  and  $1189 \text{ cm}^{-1}$ , at  $764 \text{ cm}^{-1}$  in  $\text{MnPS}_3$  and at  $1145 \text{ cm}^{-1}$  in  $\text{ZnPS}_3$ .<sup>67</sup> The other Raman modes are attributed to the cation vibration.<sup>124, 125</sup> The Raman spectra of  $\text{MPS}_3$  ( $M = \text{Mn, Fe, Co, Ni, Zn, Cd}$ ) are shown in Figure 11b. In  $\text{FePS}_3$  and  $\text{FePSe}_3$ , the intralayer modes exhibit a slighter Raman shift when the crystals thickness decreases, even to monolayers.<sup>59</sup>

Owing to the difference in the metal atoms in  $\text{MPX}_3$ , trisulphides with  $M = \text{Mn, Fe, Co, Ni}$ , undergo a paramagnetic to antiferromagnetic transition with decreasing temperature. However,  $\text{SnPS}_3$ ,  $\text{ZnPS}_3$  and  $\text{CdPS}_3$  exhibit only diamagnetic behavior. The Néel temperature can be obtained from the magnetic susceptibility measurement (as shown in Figure 12a). Within the trisulphide series, the Néel temperature increases with an increase in atomic number and the orbital component enhances the total effective magnetic moment (from the pure spin moment for Mn to the highest orbital moment for Ni).<sup>67</sup> Table 2 summarizes the Néel temperature of  $\text{MPS}_3$  ( $M = \text{Mn, Fe, Co, Ni}$ ) obtained by different measurements. When some  $\text{MPS}_3$  crystal are exfoliated down to the monolayer, the Néel temperature decreases. From Table 2, the Néel temperature of bulk  $\text{FePS}_3$  is approximately 116-120 K. Wang *et al.*<sup>65</sup> reported that the Néel temperature decreased to 104K for the  $\text{FePS}_3$  monolayers, as shown in Figures 12b-d. Furthermore, Toyoshima *et al.*<sup>66</sup> found that the pressure also affects the Néel temperature. The Néel temperature decreased from 86 K to 78K for  $\text{MnPS}_3$  bulk crystals at an applied pressure of 0.47 GPa.

### 3.2 Ternary MXenes

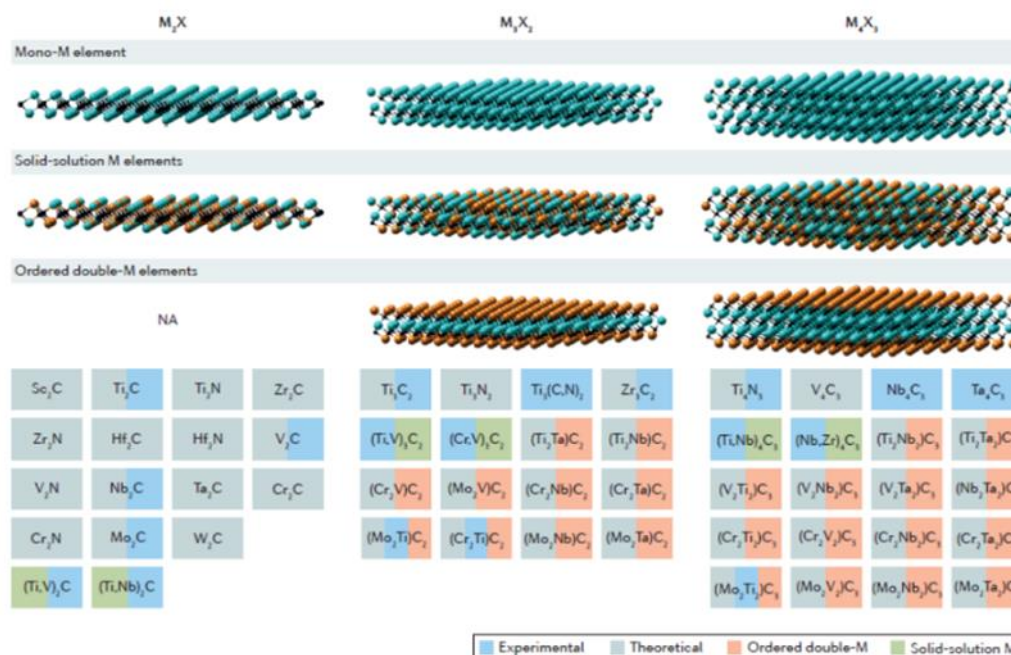


**Figure 13** MXenes reported so far. MXenes can have at least three different formulas:  $M_2X$ ,  $M_3X_2$  and  $M_4X_3$ . They can be made in three different forms: mono-M elements; a solid solution of at least two different M elements; or ordered double-M elements, Solid solutions on the X site produce carbonitrides. Reprinted from Ref. 78 with permission from Nature Publishing Group.

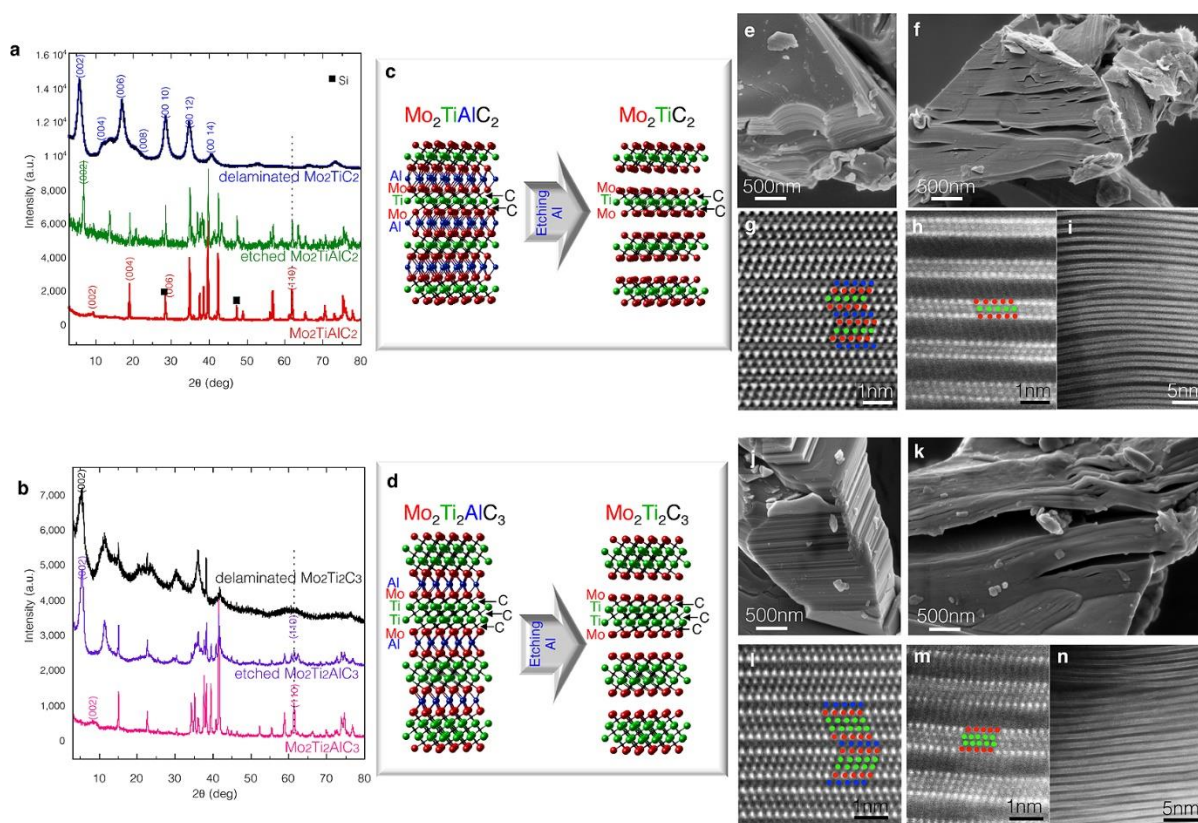


**Figure 14** Synthesis and structure of  $Mo_2TiC_2$  and  $Mo_2Ti_2C_3$ . (a) XRD patterns of  $Mo_2TiAlC_2$  before and after HF treatment and after delamination. (b) XRD patterns of  $Mo_2Ti_2AlC_3$  before and after HF treatment and after delamination. (c and d) Schematics of  $Mo_2TiAlC_2$  to  $Mo_2TiC_2$  and  $Mo_2Ti_2AlC_3$  to  $Mo_2Ti_2C_3$  transformations, respectively; (e and f) SEM images of  $Mo_2TiAlC_2$  and  $Mo_2TiC_2$ , respectively. (g and h and i) HRSTEM of  $Mo_2TiAlC_2$  and  $Mo_2TiC_2$ , respectively. (j) Lower magnification TEM image of (f) showing the layered structure throughout the sample. (k and l) SEM images of  $Mo_2Ti_2AlC_3$  and  $Mo_2Ti_2C_3$ , respectively. HRSTEM images of (l)  $Mo_2Ti_2AlC_3$  and (m and n)  $Mo_2Ti_2C_3$ . Reprinted from Ref. 130 with permission from the American Chemistry Society.

Transition metal carbides, carbonitrides and nitrides (MXenes) are a new class of 2D materials. It has a general formula of  $M_nX_{n-1}T_x$  ( $n = 2-4$ ), where M denotes early transition metals (Sc, Ti, Zr, V, Cr, Mo, etc.), X represents carbon and/or nitrogen and  $T_x$  indicates surface terminators.<sup>78, 127, 128</sup> In general, MXenes are obtained by the selective etching of the A element layers from the MAX ( $M_nAX_{n-1}$ : M = metal; A = Group IIIA or IVA elements; X = carbon and/or nitrogen) phases at room temperature.<sup>79, 129</sup> Due to the etching process, MXenes are always surface terminated with groups such as the F, OH, and O groups after its exfoliation from the MAX phase.<sup>77</sup> Figure 13 displays the structure of  $M_nX_{n-1}$ , which shows  $n$  layers of M cover with  $n-1$  layers of X in an  $[MX]_{n-1}M$  arrangement. When there is more than one metal in the structure, it exhibits in two forms: solid solutions and ordered phases. The two different metals are randomly arranged in solid solution MXenes, while in ordered phases MXenes, single or double layers of one metal are between the layers of a second metal.<sup>78</sup> Though DFT calculations, ordered MXenes have been shown to be energetically more stable than their solid-solution counterparts for certain combinations of transition metals.<sup>130</sup> More than 25 different ordered MXenes have been predicted as shown in Figure 13. In this review, we only emphasise the properties of ternary (multiple metals) MXenes. Anasori *et al.*<sup>130</sup> reported that more than 25 ternary MXenes have a stable ordered structure, based on DFT calculations. For MXenes with the  $M'_2M''C_2$  composition,  $Mo_2TiC_2$ ,  $Mo_2VC_2$ ,  $Mo_2TaC_2$ ,  $Mo_2NbC_2$ ,  $Cr_2TiC_2$ ,  $Cr_2VC_2$ ,  $Cr_2TaC_2$ ,  $Cr_2NbC_2$ ,  $Ti_2NbC_2$ ,  $Ti_2TaC_2$ ,  $V_2TaC_2$  and  $V_2TiC_2$  have a fully ordered state at 0 K. Moreover,  $Nb_2VC_2$ ,  $Ta_2TiC_2$ ,  $Ta_2VC_2$  and  $Nb_2TiC_2$  are more stable in their partially ordered state than in their fully ordered state. In contrast, MXenes with the  $M'_2M''C_3$  composition,  $Mo_2Ti_2C_3$ ,  $Mo_2V_2C_3$ ,  $Mo_2Nb_2C_3$ ,  $Mo_2Ta_2C_3$ ,  $Cr_2Ti_2C_3$ ,  $Cr_2V_2C_3$ ,  $Cr_2Nb_2C_3$ ,  $Cr_2Ta_2C_3$ ,  $Nb_2Ta_2C_3$ ,  $Ti_2Nb_2C_3$ ,  $Ti_2Ta_2C_3$ ,  $V_2Ta_2C_3$ ,  $V_2Nb_2C_3$  and  $V_2Ti_2C_3$  are ordered at 0 K. They found that the Mo and Cr atoms avoid the middle layers, whereas Ta and Nb are preferred. Furthermore, in all the cases, the total density of states (DOS) at the Fermi level ( $E_f$ ) is dominated by the M-M d-orbitals, irrespective of surface termination.

Anasori *et al.*<sup>130</sup> also synthesized  $Mo_2TiC_2$  and  $Mo_2Ti_2C_3$  by etching Al from their MAX phases ( $Mo_2TiAlC_2$  and  $Mo_2Ti_2AlC_3$ , respectively). The synthesis and structure of  $Mo_2TiC_2$  and  $Mo_2Ti_2C_3$  are shown in Figure 14. The MAX phase peaks in the XRD patterns disappeared after etching and the Al signals showed a significant drop, which confirmed the formation of MXenes. The yields of the two compounds are almost 100%. The 3D to 2D transformations in both materials were confirmed by a scanning electron microscope (SEM) and the layers opened after etching. The high-resolution scanning transmission electron microscope (HRSTEM) images of  $Mo_2TiC_2$ ,  $Mo_2Ti_2C_3$ ,  $Mo_2TiAlC_2$  and  $Mo_2Ti_2AlC_3$  clearly show the removal of the Al layers by etching.  $Mo_2TiC_2$  with surface terminators can be delaminated by first intercalating dimethyl sulfoxide (DMSO) and then sonicating in water. After

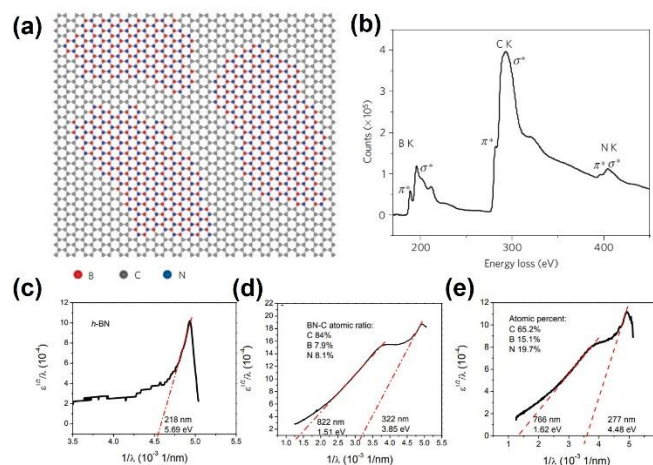


**Figure 15** (a) Atomic model of the *h*-BNC film showing hybridized *h*-BN and graphene domains. (b) K-shell excitations of B, C and N are revealed from the core EELS spectra taken from these films. Optical absorption data from the *h*-BN sample(a), *h*-BNC sample with 84at.% C (b), and *h*-BNC sample with 65at.% C (c). Reprinted from Ref. 22 with permission from Nature Publishing Group.

delamination, a stable colloidal solution is obtained, which can be used to form freestanding conductive papers.

Khazaei *et al.*<sup>131</sup> found that  $M'_2M''C_2$  ( $M' = Mo, W$ ;  $M'' = Ti, Zr, Hf$ ) with  $O_2$  as the surface terminator are topological insulators.  $W_2HfC_2O_2$  shows the largest band gap (0.285 eV). Such large band gaps pave the way for the practical applications of topological insulators at room temperature. Furthermore,  $M'_2M''C_3O_2$  ( $M' = Mo, W$ ;  $M'' = Ti, Zr$ ) are topological semi-metals. The first Sc-containing MAX phase was reported by Meshkian *et al.*<sup>132</sup> very recently.  $Mo_2ScC_2$  MXene is obtained by the selective etching of the Al-layers in hydrofluoric acid. It expands the attainable range of MXene compositions and widens the prospects for property tuning.

### 3.4 BCN and other ternary 2D materials

The *h*-BCN system is another important type of ternary 2D materials. Theoretical calculations<sup>92</sup> indicates that homogenous *h*-BCN tends to form graphene and *h*-BN domains separately (Figure 15a). So far, a homogeneous ternary BCN without phase separation has not been realized. The chemical composition and structure of *h*-BCN can be analyzed by electron energy-loss spectroscopy (EELS). Three visible edges of *h*-BCN films were observed, starting at 185, 276 and 393 eV (Figure 15b), which corresponded to the characteristic K-shell ionization edges of B, C and N, respectively.<sup>22, 133</sup> Furthermore, such types of EELS edge structures indicates that all three elements are  $sp^2$  hybridized<sup>133</sup>. Owing to domain separation, the band gap engineering can be tuned by controlling the concentration of carbon. The optical band gap of *h*-BCN with different domain concentrations was measured by ultraviolet-visible absorption spectra (Figures 15c-e). The *h*-BN sample shows one absorption edge at 218 nm, which corresponds to an

optical band gap of 5.69 eV (Figure 15c). With C concentrations of 65 at.% and 84 at.%, the band gaps are 4.48

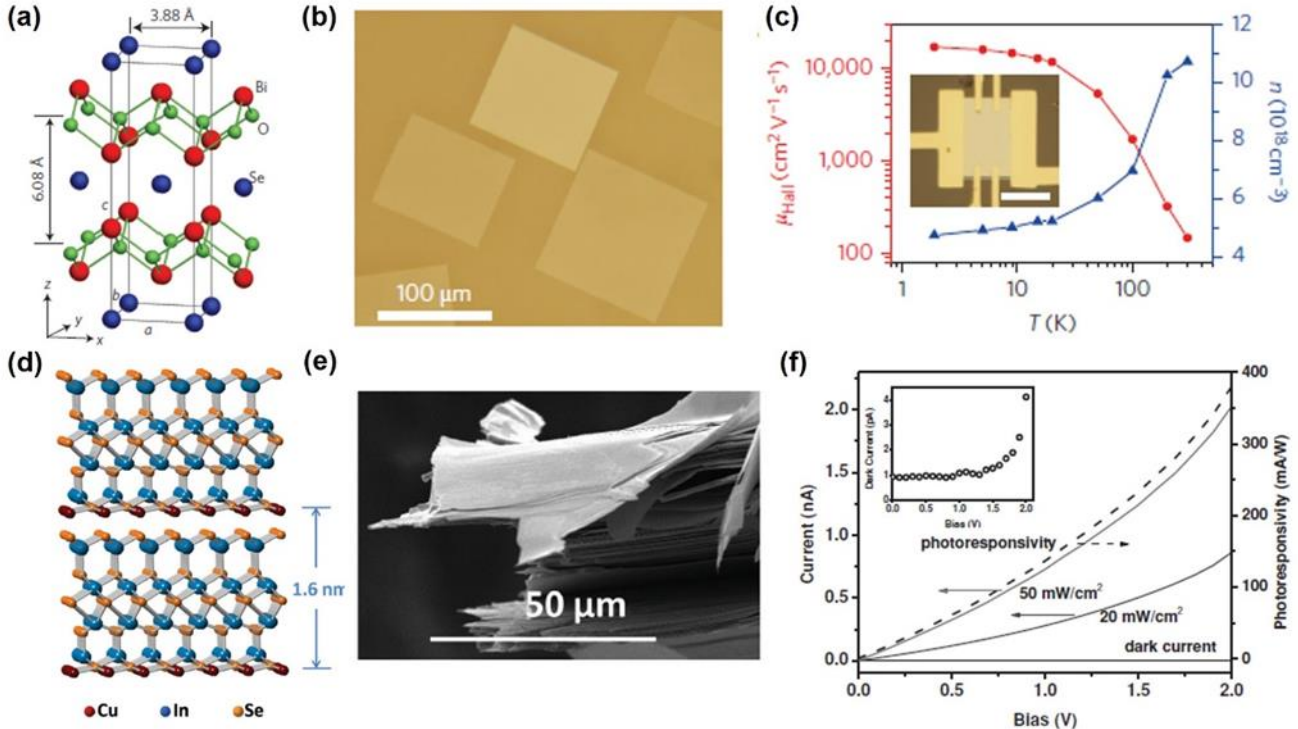


**Figure 16** (a) Layered crystal structure of  $\text{Bi}_2\text{O}_2\text{Se}$  with tetragonal  $(\text{Bi}_2\text{O}_2)_n$  layers and  $\text{Se}_n$  layers alternately stacked along the  $c$  axis. (b) Typical optical microscopy image of square  $\text{Bi}_2\text{O}_2\text{Se}$  nanoplates grown on mica. (c) Hall mobility and carrier density as a function of temperature in a  $\text{Bi}_2\text{O}_2\text{Se}$  nanoplate. Inset: optical microscopy image of a Hall-bar device fabricated on the  $\text{Bi}_2\text{O}_2\text{Se}$  nanoplate with a thickness of  $\sim 20.9$  nm. (a-c) Reprinted from Ref. 134 with permission from Nature Publishing Group. (d) Crystal structure model of  $\text{CuIn}_7\text{Se}_{11}$ . A single-layered  $\text{CuIn}_7\text{Se}_{11}$  contains 5 layers of metallic ions. (e) Scanning electron microscope (SEM) image of a  $\text{CuIn}_7\text{Se}_{11}$  crystal. (f) Photoconductivity IV curves of  $\text{CuIn}_7\text{Se}_{11}$  photodetector. (d-f) Reprinted from Ref. 25 with permission from Wiley.

and 3.85 eV, respectively. This indicates that the band gap decreases with a decrease in the h-BN domain. Furthermore, a second absorption edge was observed, which corresponds to the optical band gap of 1.62 and 1.51 eV from the samples with 65 and 84 at.% C, respectively. This absorption edge can be assigned to the h-BN-doped graphene domains.

Wu *et al.*<sup>134</sup> reported a new ternary 2D material ( $\text{Bi}_2\text{O}_2\text{Se}$ ) with an ultrahigh Hall mobility of  $>20,000 \text{ cm}^2\text{V}^{-1}\text{s}^{-1}$  at low temperatures. It shows a tetragonal structure with the  $I4/mmm$  space group and consists of  $\text{Bi}_2\text{O}_2$  planar covalent layers sandwiched by Se atoms with relatively weak electrostatic interactions (Figure 16a). It does not show standard van der Waals gaps compared with TMDs. Therefore, the cleavage should be along the Se planes, which results in a possible rearrangement of the surface atomic structure.  $\text{Bi}_2\text{O}_2\text{Se}$  preferentially crystallizes onto a mica substrate with a large lateral size. Figure 16b shows the morphology of  $\text{Bi}_2\text{O}_2\text{Se}$ , which exhibits a square shape and ultra-flat surfaces. The temperature dependence of Hall mobility is shown in Figure 16c.  $\text{Bi}_2\text{O}_2\text{Se}$  flakes exhibit the electron Hall mobility of  $18,500\text{--}28,900 \text{ cm}^2\text{V}^{-1}\text{s}^{-1}$  at 1.9 K. Lei *et al.*<sup>25</sup> reported another ternary copper indium selenide 2D material ( $\text{CuIn}_7\text{Se}_{11}$ ) with good photo-response. The side view of the  $\text{CuIn}_7\text{Se}_{11}$  structure is shown in Figure 16d. The inter-layer distance in this material is 1.6 nm and it shows standard van der Waals gaps between layers. This layer structure is confirmed by SEM, as shown in

Figure 16e, which indicates a weak interlayer interaction. Figure 16f shows the photo-response of the few-layer  $\text{CuIn}_7\text{Se}_{11}$ . The dark current of the device is in the order of 1 pA, which is very low compared to most layered material based photodetectors.<sup>27, 33</sup> When  $\text{CuIn}_7\text{Se}_{11}$  is illuminated by a 543-nm laser with intensities of  $20 \text{ mW}/\text{cm}^2$  and  $50 \text{ mW}/\text{cm}^2$ , the device shows a strong photo-response.

Very recently, Gong *et al.*<sup>135</sup> reported a long-range ferromagnetic order in pristine  $\text{Cr}_2\text{Ge}_2\text{Te}_6$  Van der Waals crystals. By the investigation of the temperature and magnetic-field-dependent Kerr effect via scanning magneto-optic Kerr microscopy, the ferromagnetic transition temperature was controlled. The crystal structure (side and top views) of  $\text{Cr}_2\text{Ge}_2\text{Te}_6$  is shown in Figure 17(a).  $\text{Cr}_2\text{Ge}_2\text{Te}_6$  is a new layered material belonging to the lamellar ternary  $\text{M}_2\text{X}_2\text{Te}_6$  chalcogenides family (where M donates a +3 oxidation state metal and  $\text{X}_2$  represents a silicon or a germanium pair). It has an interlayer Van der Waals spacing of 3.4 Å. Schematic representations of the magnon density of states per spin around the low-energy band edge of the monolayer, multi-layer and bulk ferromagnetic materials are presented in Figures 17b-d. These figures show that the density of states per spin for the magnon modes near the excitation gap is rapidly reduced. Figure 17e shows the transition temperatures  $T_c$  of samples of different thicknesses, obtained from the Kerr measurements (blue squares) and theoretical calculations (red circles). A strong dimensionality

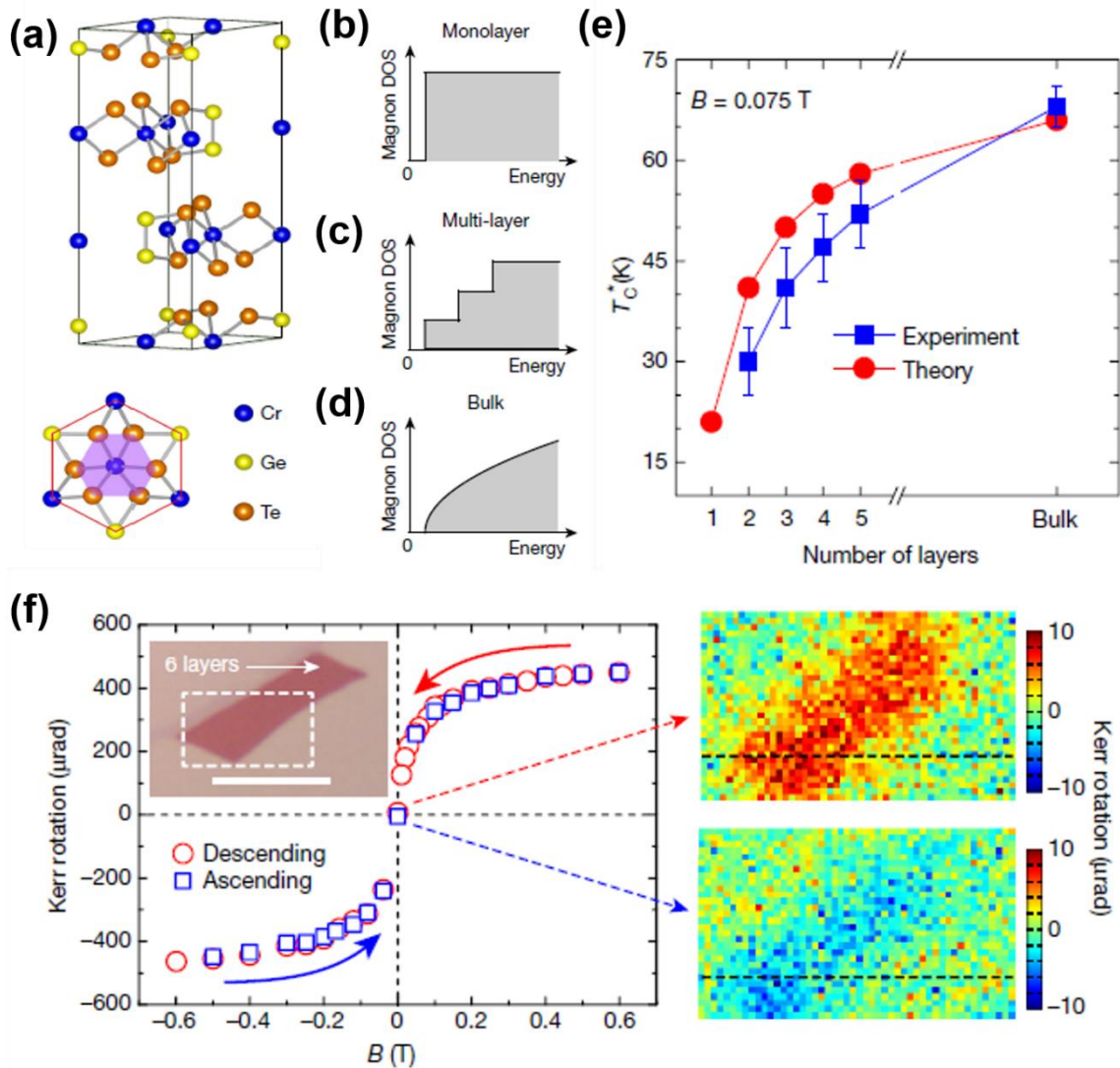


**Figure 17** (a) Crystal structure (side and top views) of Cr<sub>2</sub>Ge<sub>2</sub>Te<sub>6</sub>. (b-d) Schematics of magnon density of states (DOS) per spin around the low-energy band edge of monolayer (b), multi-layer (c) and bulk (d) ferromagnetic materials. (e) Transition temperatures  $T_c^*$  (defined in text) of samples of different thickness, obtained from Kerr measurements (blue squares) and theoretical calculations (red circles). (f) Hysteresis loop of a six-layer flake at 4.7 K showing a saturating trend at 0.6 T and small non-vanishing remanence. The solid red (blue) arrow represents the descending (ascending) field. The loop starts from 0.6 T. Inset, optical image of the flake; scale bar, 10 μm. Reprinted from Ref. 135 with permission from Nature Publishing Group.

effect is observed, in line with the experimental observations. A ferromagnetic hysteresis loop with single-domain remanence in a six-layer Cr<sub>2</sub>Ge<sub>2</sub>Te<sub>6</sub> crystal is shown in Figure 17f. The almost saturated Kerr signal at 0.6 T shows approximately 75 μrad per layer. Under a magnetic field, there is a clear contrast between the insensitivity of the transition temperature of the three-dimensional system. By using the renormalized spin wave theory to analyze the observed phenomena, we concluded that the relationship between the transition temperature and the magnetic field is the intrinsic specificity of the 2D ferromagnetic molecular crystal. In this 2D molecular ferromagnetic material, for the first time, a very small magnetic field (less than 0.3 T) was used to achieve transition

temperature (ferromagnetic and paramagnetic state transition between the temperatures) regulation. Their experimental observations may provide a generic understanding of the ferromagnetic behavior of many soft, 2D van der Waals ferromagnets, such as Cr<sub>2</sub>Si<sub>2</sub>Te<sub>6</sub> and CrI<sub>3</sub>.

## 4 Potential applications

### 4.1 Energy storage

Energy storage is an important application of 2D materials. Batteries and supercapacitors are two main types of energy storage devices. Extensively studies have been reported for binary 2D materials; however, as far as we know, only a few

reports have been published for ternary 2D materials. Since their discovery, MXenes have been explored for use as anodes

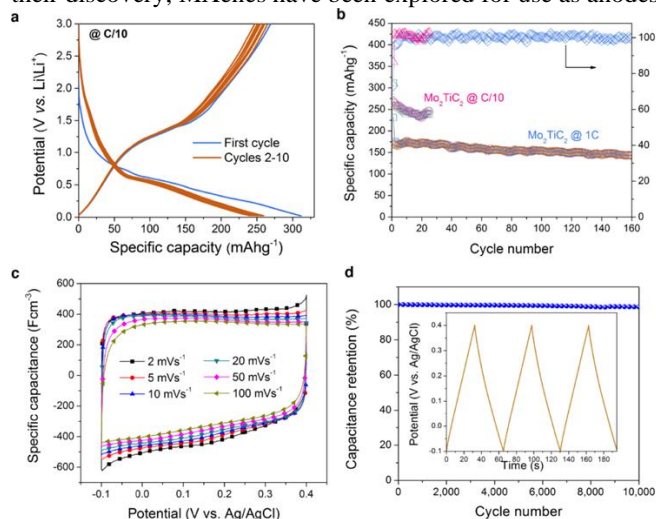


**Figure 18** Electrochemical performance of  $\text{Mo}_2\text{TiC}_2$  in LIB and supercapacitor electrodes. (a) Voltage profiles between 0.02 and 3 V vs  $\text{Li}/\text{Li}^+$  at C/10 rate for the first 10 cycles. (b) Specific lithiation (squares) and delithiation (circles) capacities versus cycle number at 1 C and C/10 rates. Right axis in panel (b) shows the Coulombic efficiencies for cells tested at these rates. (c) Cyclic voltammograms, at different scan rates, for a freestanding electrode in 1 M  $\text{H}_2\text{SO}_4$ . (d) Capacitance retention test of  $\text{Mo}_2\text{TiC}_2$  'paper' in 1 M  $\text{H}_2\text{SO}_4$ . Inset shows galvanostatic cycling data collected at a current density of 1 A/g. Reprinted from Ref. 130 with permission from the American Chemistry Society.

in lithium-ion batteries (LIBs) and sodium-ion batteries (SIBs) as well as for supercapacitors and pseudo-capacitor applications owing to their promising features such as sufficiently large electrochemically active surfaces excellent electrical conductivity, exceptional mechanical properties and tunable band gap energies. In addition, the structure of layered MXenes not only allows the intercalation of a variety of organic and inorganic molecules/ions but also disperses easily in aqueous solutions (hydrophilic)<sup>128, 136-139</sup>. DFT calculation predicts that a higher formula unit of MXenes leads to a fast diffusion rate but low reversible capacity as compared to that of the lower formula unit, and vice versa.<sup>140</sup> Ternary MXenes, in accordance with their binary analogues, exhibit a striking ability to store  $\text{Li}^+/\text{Na}^+$  and exhibit a superior specific capacity with improved stability.

To date, limited ternary MXene materials, such as  $\text{Mo}_2\text{ScC}_2$ ,  $(\text{Nb}_{0.8}\text{Ti}_{0.2})_4\text{C}_3\text{T}_x$  and  $(\text{Nb}_{0.8}\text{Zr}_{0.2})_4\text{C}_3\text{T}_x$ ,<sup>132, 138, 141</sup> have been studied for energy storage applications. Barsoum *et al.*<sup>142</sup> reported two  $\text{Nb}_4\text{AlC}_3$ -based solid solution MAX phases  $(\text{Nb}_{0.8}\text{Ti}_{0.2})_4\text{AlC}_3$  and  $(\text{Nb}_{0.8}\text{Zr}_{0.2})_4\text{AlC}_3$ , and their corresponding MXenes,  $(\text{Nb}_{0.8}\text{Ti}_{0.2})_4\text{C}_3\text{T}_x$  and  $(\text{Nb}_{0.8}\text{Zr}_{0.2})_4\text{C}_3\text{T}_x$ , were synthesized. Substituting 20 at.% of Nb atoms with Ti or Zr atoms did not result in significant changes in the Li uptake compared with  $\text{Nb}_4\text{C}_3\text{T}_x$ .  $(\text{Nb}_{0.8}\text{Ti}_{0.2})_4\text{C}_3\text{T}_x$  and  $(\text{Nb}_{0.8}\text{Zr}_{0.2})_4\text{C}_3\text{T}_x$  retained the specific capacities of 158 and 132 mAh/g after 20 cycles, respectively.

Barsoum *et al.*<sup>130</sup> synthesized  $\text{Mo}_2\text{TiC}_2$ ,  $\text{Mo}_2\text{Ti}_2\text{C}_3$  and  $\text{Cr}_2\text{TiC}_2$  ternary MXenes, and explored the potential of  $\text{Mo}_2\text{TiC}_2$  with respect to electrochemical energy storage. The  $\text{Mo}_2\text{TiC}_2\text{T}_x$

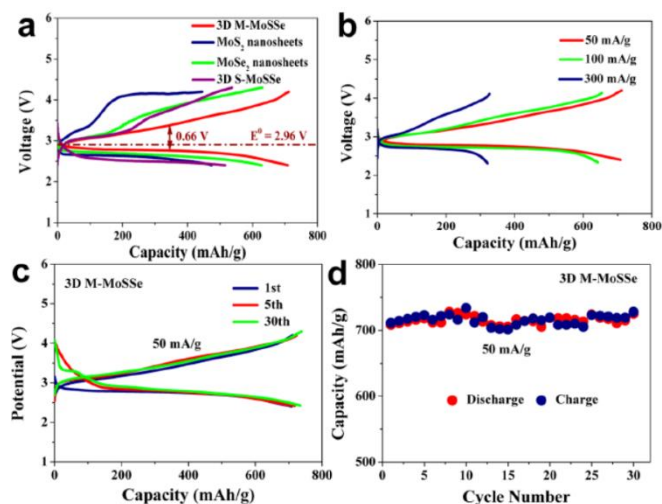


**Figure 19** (a) The first cycle discharge-charge profile of the  $\text{MoS}_2$ ,  $\text{MoSe}_2$ , 3D S-MoSSe, and 3D M-MoSSe cathode at a current density of  $50 \text{ mA g}^{-1}$ . (b) Galvanostatic discharge and charge curves of the 3D metastable MoSSe cathode in the first cycle at current densities from 50 to  $300 \text{ mA g}^{-1}$ . (c) Full discharge-charge profiles of the Li-O<sub>2</sub> batteries with 3D M-MoSSe cathode. (d) The cycling stability of the Li-O<sub>2</sub> cell with 3D metastable MoSSe cathode. Reprinted from Ref. 148 with permission from the American Chemistry Society.

electrode showed a stable capacity of about 176 mAh/g in the second cycle and retained about 82% of this capacity after 160 cycles (Figure 18). About 92% of the 260 mAh/g capacity was retained after 25 cycles at C/10. At both rates, Coulombic efficiencies higher than 97% were observed after the first cycle. Considering that more than 20 theoretically predicted members belong to the ternary system, further exploration regarding electrochemical performance with various MXenes is expected. As early as 1977, Thompson *et al.*<sup>143</sup> reported that  $\text{NiPS}_3$  was used as a cathode in the Li-ion battery.  $\text{NiPS}_3$  has a capacitance of 1 kWh/kg and a capacity retention of 30% after 300 cycles. Following this, Kuz'minskii *et al.*<sup>144</sup> investigated the electrochemical properties of the layered  $\text{NiPS}_3$  compound at  $200^\circ\text{C}$ . They found that the reversible behavior of the  $\text{NiPS}_3$  electrode was possible during the charge/discharge cycles within the  $0 \leq \text{Li}/\text{Ni} \leq 3$  range.

Even though numerous reports on binary TMDs for the applications of batteries and supercapacitors have been published,<sup>50, 145-147</sup> limited research was found on ternary TMDs. Zhang *et al.*<sup>148</sup> developed a novel and effective strategy to distort the lattice structure of MoSSe and tune its properties for Li-O<sub>2</sub> batteries (Figure 19). The Li-O<sub>2</sub> batteries can deliver a high discharge capacity of 708.24 mAh/g for a metastable MoSSe solid solution at the current density of  $50 \text{ mA/g}$ . Further, they also showed a high specific capacity of  $\sim 730 \text{ mAh/g}$  with stable discharge-charge overpotentials (0.17/0.49V) over 30 cycles.

## 4.2 Electrocatalysts

Hydrogen is the most environmentally friendly fuel with the largest energy density, and may be the world's primary fuel source in the future.<sup>149</sup> However, hydrogen is not found naturally in the high-density gas form.<sup>127</sup> Water splitting is an

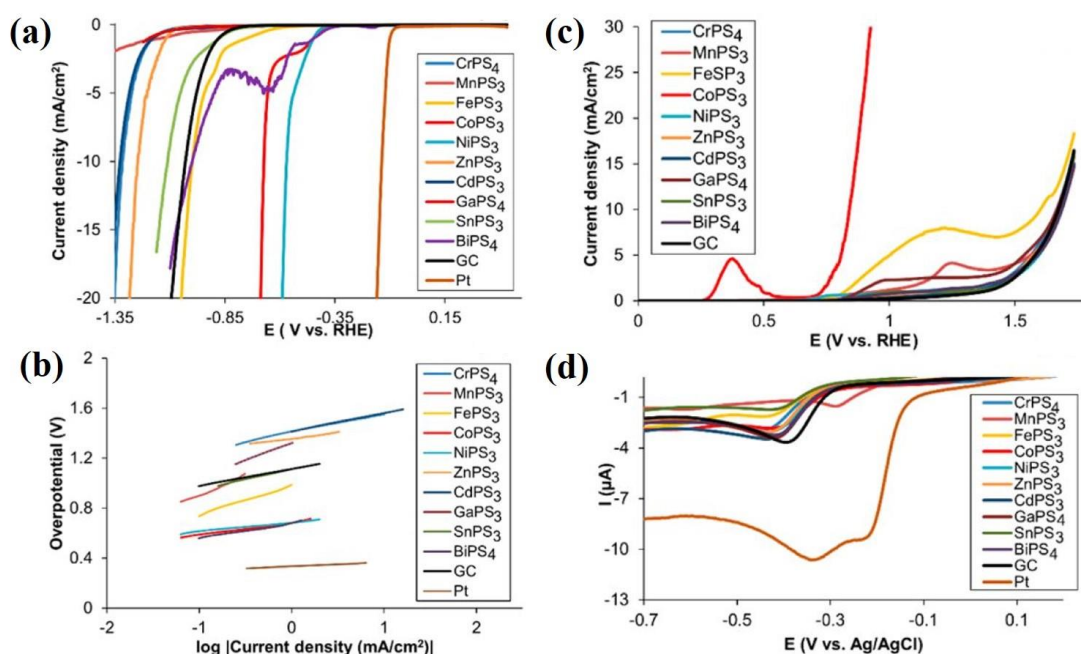


**Figure 20** Linear sweep voltammograms (a) and Tafel plots (b) of hydrogen evolution reaction (HER) of several MPTs. LSV of oxygen evolution reaction (OER) (c) and LSV of oxygen reduction reaction (ORR) (d) of several MPTs. Reprinted from Ref. 67 with permission from the American Chemistry Society.

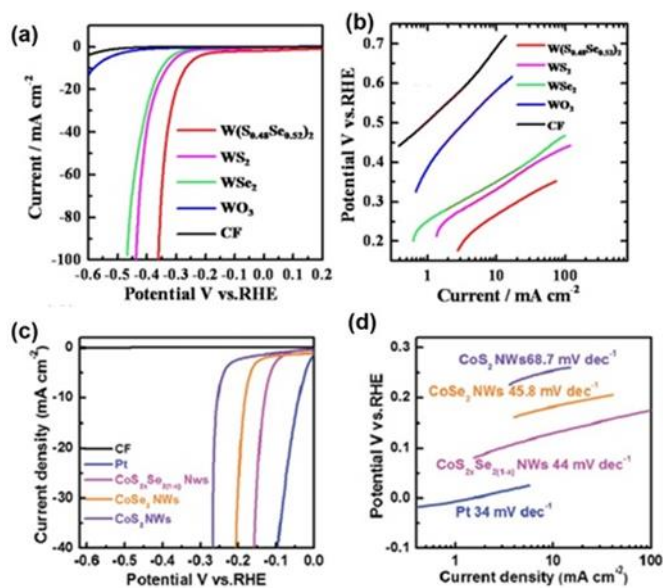


**Figure 21** Linear sweep voltammograms (a) and Tafel plots (b) of hydrogen evolution reaction (HER) for  $W_{2x}Se_{2(1-x)}$ . (a-b) Reprinted from Ref. 156 with permission from the American Chemistry Society. Linear sweep voltammograms (c) and Tafel plots (d) of hydrogen evolution reaction (HER) for  $CoS_{2x}Se_{2(1-x)}$ . (c-d) Reprinted from Ref. 157 with permission from the Royal Society of Chemistry.

important clean energy technology to produce hydrogen. It involves the oxygen evolution reaction (OER) ( $2H_2O \rightarrow 4e^- + 4H^+ + O_2$ ) and hydrogen evolution reaction (HER) ( $2H^+ + 2e^- \rightarrow H_2$ ). Platinum is the most efficient catalyst for HER (Tafel slope: 29 mV/dec).<sup>54</sup> However, platinum is quite expensive and the resource is limited, therefore, the usage is restricted.<sup>150-152</sup> Despite the fact that many binary MXenes works have been reported on the HER application,<sup>153-155</sup> the reports on ternary

MXenes are rather rare. In this section, we emphasize MPTs and TTMDs.

From DFT calculations,<sup>122</sup> metal phosphorus trichalcogenides were found to have the potential to be used in HER and OER. Pumera *et al.*<sup>67</sup> reported HER, OER and oxygen reduction reaction (ORR) for several metal phosphorus trichalcogenides (Figure 20). The onset potentials of  $NiPS_3$  (-0.53 V vs. RHE),  $CoPS_3$  (-0.59 V vs. RHE), and  $FePS_3$  (-0.86 V vs. RHE) lie between the onset potentials of Pt (-0.103 V vs. RHE) and glassy carbon (GC) (-0.89 V vs. RHE). The high HER activity for  $NiPS_3$  and  $CoPS_3$  may be attributed to the crystal structure. The highest catalytic efficiency was observed for  $NiPS_3$  with a Tafel slope at an average of ~56 mV/dec. In addition,  $ZnPS_3$  (75 mV/dec) and  $CoPS_3$  (84 mV/dec) have a Tafel slope less than 100 mV/dec. The best catalytic performance for OER was observed on  $CoPS_3$  with an onset potential of 0.84 V at 10 mA/cm<sup>2</sup>, and the current density reached 30 mA/cm<sup>2</sup>. However, other materials exhibited lower OER activities. The best performance of ORR is observed in  $MnPS_3$ . The reduction peak was at about -0.28 V vs. RHE, while for Pt the reduction peak was at about -0.21 V vs. RHE.

Various binary TMDs, particularly  $MoS_2$  and  $WS_2$ , have been confirmed to be efficient non-Pt catalysts for HER.<sup>158-163</sup> It is easy to tune the electronic structure of  $MS_{2x}Se_{2(1-x)}$  (M=Mo, W, Co) upon Se/S incorporation, which probably further assists in the realization of high HER activity.<sup>54, 62, 108</sup> Kiran *et al.*<sup>62</sup> reported the HER properties of  $MoSSe$ .  $MoSSe$  has a more positive onset potential for HER than the few-layer pristine  $MoS_2$  and  $MoSe_2$  nanosheets. A typical Tafel slope obtained for

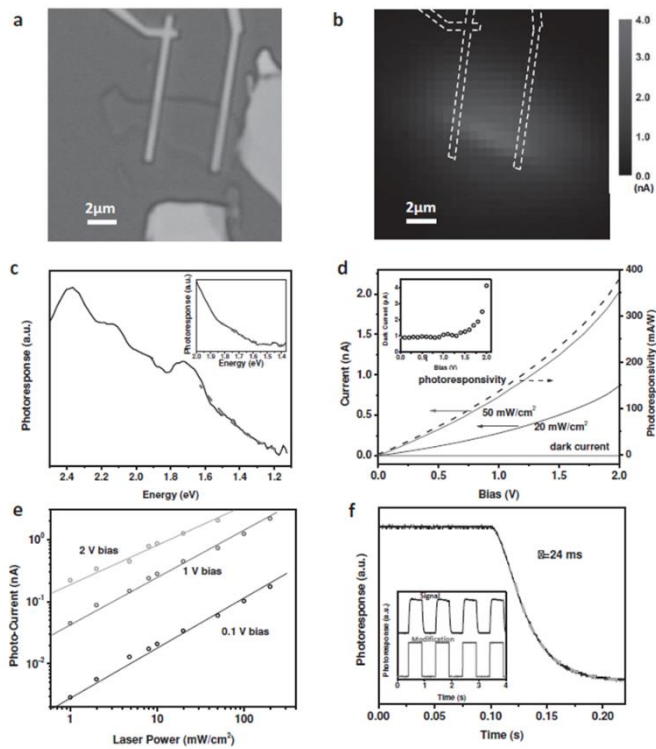


**Figure 22** Photoresponse study of mechanically exfoliated CIS few layered samples. (a) Optical image of a 3–4 layered CIS flake photodetector. (b) The photocurrent mapping of the as-fabricated CIS photo-detector. (c) The photoconductivity spectrum of a 3–4 layered CIS sample with 2  $\mu\text{m}$  electrode spacing indicates an indirect band-gap of 1.1 eV, while a 1–2 layered sample (inset) has a larger band gap of 1.4 eV. (d) Photoconductivity IV curves of CIS photodetector. (e) The photoresponse is linear as a function of illumination intensity with a 0.1, 1, and 2 V bias. The illumination intensity ranges from 0 to 200  $\text{mW cm}^{-2}$  and the current varies from 1 pA (dark current) to 2.16 nA, yielding a linear response range larger than 70 dB. (f) The time-resolved photoresponse measurement illustrates a stable photoresponse performance with a time constant of 24 ms. Reprinted from Ref. 25 with permission from Wiley.

MoSSe is 56 mV/dec, which is quite smaller than that of MoS<sub>2</sub> (96 mV/dec) and MoSe<sub>2</sub> (95 mV/dec). Konkena *et al.*<sup>54</sup> synthesized MoSSe@reduced graphene oxide (r-GO) nanocomposite heterostructures to further improve the HER performance. The onset potential of the MoSSe@r-GO composite nanostructures further positively shifted. The enhanced catalytic activity was realized owing to the superior electron transfer efficiency caused by the electronic conductivity of r-GO. The Tafel slopes of the MoSSe@rGO composite and MoSSe are 51 and 63 mV/dec, respectively. Such low Tafel slopes indicate faster reaction kinetics during hydrogen evolution than in the case of MoSS nanosheets.

Xu *et al.*<sup>156</sup> synthesized WS<sub>2</sub>xSe<sub>2(1-x)</sub> nanotubes and investigated the HER performance. MoS<sub>2</sub>xSe<sub>2(1-x)</sub> ( $x = 0.48$ ) shows the best HER catalytic activity among all electrocatalysts shown in Figure 21a. Both the increased number of active sites and higher conductivity of MoS<sub>2</sub>xSe<sub>2(1-x)</sub> ( $x = 0.48$ ) are responsible for the good HER performance. The Tafel slopes (Figure 21b) of the WSe<sub>2</sub> and MoS<sub>2</sub>xSe<sub>2(1-x)</sub> ( $x = 0.48$ ) are 99

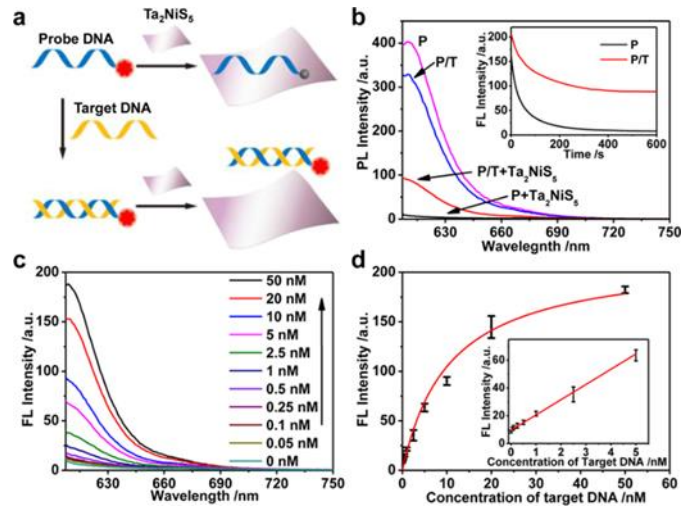


**Figure 23** Single-layer Ta<sub>2</sub>NiS<sub>5</sub> nanosheet-based fluorescence sensor for DNA detection. (a) Schematic illustration of the DNA detection based on single-layer Ta<sub>2</sub>NiS<sub>5</sub> nanosheets. (b) Fluorescence spectra of P (10 nM) and P/T (10 nM) in the absence and presence of single-layer Ta<sub>2</sub>NiS<sub>5</sub> nanosheets. Inset: The fluorescence quenching curves of P and P/T in the presence of single-layer Ta<sub>2</sub>NiS<sub>5</sub> nanosheet (4.0  $\mu\text{g/mL}$ ). (c) Fluorescence spectra of P in the presence of different concentrations of T (0, 0.05, 0.1, 0.25, 0.5, 1, 2.5, 5, 10, 20, 50 nM) with addition of single-layer Ta<sub>2</sub>NiS<sub>5</sub> nanosheet (4.0  $\mu\text{g/mL}$ ). (d) Calibration curve of DNA detection. Inset: The linear plot of fluorescence peak intensity of P vs the concentration of T with addition of single-layer Ta<sub>2</sub>NiS<sub>5</sub> nanosheet (4.0  $\mu\text{g/mL}$ ). The excitation and emission wavelengths are 596 and 610 nm, respectively. Reprinted from Ref. 23 with permission from the American Chemistry Society.

and 105 mV/dec, respectively, which are lower than WS<sub>2</sub> (113 mV/dec).<sup>164</sup> Liu *et al.*<sup>157</sup> presented the HER performance of CoS<sub>2</sub>xSe<sub>2(1-x)</sub> nanowires (Figure 21c and 21d). MoS<sub>2</sub>xSe<sub>2(1-x)</sub> ( $x = 0.67$ ) shows a more positive onset potential for HER than the CoS<sub>2</sub> and CoSe<sub>2</sub> nanowires. The linear parts of the Tafel plots reveal a low Tafel slope of 44 mV/dec for MoS<sub>2</sub>xSe<sub>2(1-x)</sub> ( $x = 0.67$ ), which is lower than that of CoS<sub>2</sub> (68.7 mV/dec) and CoSe<sub>2</sub> (45.8 mV/dec). This may be due to the optimal electronic structure of the catalyst incorporating S and Se atoms.<sup>165</sup>

### 4.3 Other applications

Owing to their unique structure and properties, ternary 2D systems are a good candidate for investigating device applications, such as photodetectors, solar cells, sensors and FETs. Thus, it is important to fabricate high-performance device using ternary 2D materials. Ternary copper indium selenide has a high photoresponsivity and wide spectral response range, and it has been intensively investigated for application in photodetectors. Ajayan *et al.* successfully synthesized and isolated high-quality few-layered flakes of ternary CuIn<sub>7</sub>Se<sub>11</sub>, and characterized its photocurrent properties using photoconductivity measurements (Figure 22).<sup>25</sup> Atomically layered CuIn<sub>7</sub>Se<sub>11</sub> (CIS) with Ti/Au electrodes shows an excellent photoresponse with a low dark current of 1 pA, an S/N larger than 95 dB for 1  $\text{mW cm}^{-2}$  543-nm illumination, a relatively fast response time of 24 ms and a large linear dynamic range of 70 dB. These properties indicate

that atomically layered  $\text{CuIn}_7\text{Se}_{11}$  is a very good candidate for 2D photodetectors. Further, they demonstrated 2D  $\text{CuIn}_7\text{Se}_{11}$  photovoltaic devices based on an asymmetric Schottky junction architecture. They observed a 2D photovoltaic effect with a power efficiency of 0.04% and an IPCE of 1.7%. This device performance can be readily improved by optimizing the electrode materials and channel lengths. Their study shows that layered  $\text{CuIn}_7\text{Se}_{11}$  is a highly promising ternary platform for atomically layered optoelectronic device development.

The electronic and photo-responsive properties of atomically thin ReSSe were reported by Liu *et al.*<sup>109</sup> They made an n-type few-layered ReSSe transistor, and the electron mobility was found to be about  $3 \text{ cm}^2\text{V}^{-1}\text{s}^{-1}$ . Because of the direct band gap nature of ReSSe, photosensitive devices based on few-layer ReSSe exhibit a very high photo-responsivity, up to  $8 \text{ AW}^{-1}$ . In combination with large-area material preparation methods such as liquid scale exfoliation or chemical vapour deposition, the composition-dependent band gaps of ReSSe alloys make ReSSe a promising material for optoelectronic applications and could enable the fabrication of low-cost and efficient optoelectronic devices.

The fabrication of high-yield and large-scale ultrathin 2D ternary chalcogenide nanosheets in solution by exfoliation of their layered microflakes, including  $\text{Ta}_2\text{NiS}_5$  and  $\text{Ta}_2\text{NiSe}_5$ , was reported.<sup>23</sup> Single-layer  $\text{Ta}_2\text{NiS}_5$  nanosheets with a yield of approximately 86% were obtained. Due to its high fluorescence quenching ability, a novel fluorescent sensor for the detection of DNA was developed on the basis of single-layer  $\text{Ta}_2\text{NiS}_5$  nanosheets. It showed excellent selectivity and sensitivity with a detection limit of 50 pM, which is better than that of the single-layer  $\text{MoS}_2$ -based biosensor (Figure 23). This highly selective and sensitive biosensor might be used for real sample analysis in the near future.

## 4 Summary and outlook

This review summarizes recent work on various ternary 2D materials, including MTPs, ternary MXene, ternary TMD and other ternary 2D materials, regarding synthetic methods, structures, key properties (band gap tuning, phase transition and topological phase) and the potential applications. Ternary 2D systems provide additional degrees of freedom to tailor the band gap tuning and physical properties via stoichiometric engineering. As such, the layered ternary 2D system is an ideal platform for this line of research. However, to realize the practical device applications, such as FETs, sensors and photodetectors, more effort is required to address the numerous issues related to the synthesis of materials. Technologies need to be developed to make high-quality layers ternary 2D materials with controlled layer numbers, size and homogeneity. In the present, as described in the growth section, most ternary 2D materials are obtained by CVT and mechanical exfoliation methods. For instance, new ternary phase ZrSTe has been grown using the CVT technique, few layered ReSSe and  $\text{PbSnS}_2$  thin films are obtained by mechanical exfoliation from single crystal, and the most commonly adopted method of

synthesizing MPTs is also realized by CVT method. Given the advantage of CVD method used in the binary 2D system, we may predict one promising direction in this field is CVD growth high quality and large size few layer ternary 2D crystals with controlled numbers. However, there are many challenges to produce single-layer and few-layer ternary 2D material by CVD method because the control of three elements is more difficult than binary ones. These need the efforts of more researchers. Meanwhile, approaches to control the composition of ternary 2D materials also need to be developed. For applications, for instance, studies on energy storage for ternary 2D materials are very limited. In this case, ternary MXenes show a striking ability to store  $\text{Li}^+/\text{Na}^+$  and exhibit a superior specific capacity with improved stability compared to their binary systems. The distinctive properties of ternary MXene sheets make them promising candidates for electrode materials in LIBs and supercapacitors. Therefore, to further investigate the properties of the ternary MXenes, it is imperative and indispensable to obtain single- or few-layers in the production by the exfoliation-intercalation method. As we reviewed above, ternary 2D systems are a good candidate for investigating device applications (photodetectors, solar cells, sensors and FETs). Thus, it is important to fabricate the high-performance device using ternary 2D materials. Especially, ternary heterostructure device has not been realized. They are expected to show high performance in photodetectors or other unique applications. In summary, for ternary 2D materials, the synthesis, potential applications, optical properties and fundamental physical properties all await further research efforts and increased understanding. We believe that ternary 2D materials are great candidates for application, and we hope more researchers will explore this area of materials and produce significant scientific developments.

## Acknowledgements

This work was financially supported by the National Natural Science Foundation of China (No. 51702203) and the Singapore National Research Foundation under NRF RF Award No. NRF-RF2013-08; MOE Tier 2 grant MOE2015-T2-2-007, MOE2016-T2-1-131, MOE2016-T2-2-153.

## Notes and references

1. K. S. Novoselov, A. K. Geim, S. V. Morozov, D. Jiang, Y. Zhang, S. V. Dubonos, I. V. Grigorieva and A. A. Firsov, *Science*, 2004, **306**, 666-669.
2. S. Bae, H. Kim, Y. Lee, X. F. Xu, J. S. Park, Y. Zheng, J. Balakrishnan, T. Lei, H. R. Kim, Y. I. Song, Y. J. Kim, K. S. Kim, B. Ozyilmaz, J. H. Ahn, B. H. Hong and S. Iijima, *Nat. Nanotechnol.*, 2010, **5**, 574-578.
3. M. C. Hu, Z. H. Yao and X. Q. Wang, *Ind. Eng. Chem. Res.*, 2017, **56**, 3477-3502.
4. F. Withers, T. H. Bointon, M. F. Craciun and S. Russo, *ACS Nano*, 2013, **7**, 5052-5057.

5. B.-M. Goh, Y. Wang, M. V. Reddy, Y. L. Ding, L. Lu, C. Bunker and K. P. Loh, *ACS Appl. Mater. Interfaces*, 2014, **6**, 9835-9841.
6. K. M. F. Shahil and A. A. Balandin, *Nano Lett.*, 2012, **12**, 861-867.
7. T. J. Echtermeyer, S. Milana, U. Sassi, A. Eiden, M. Wu, E. Lidorikis and A. C. Ferrari, *Nano Lett.*, 2016, **16**, 8-20.
8. J. Chen, Y. Wang, J. Cao, Y. Liu, Y. Zhou, J. H. Ouyang and D. Jia, *ACS Appl Mater Interfaces*, 2017, **9**, 19831-19842.
9. A. Subrati, S. Mondal, M. Ali, A. Alhindi, R. Ghazi, A. Abdala, D. Reinalda and S. Alhassan, *Ind. Eng. Chem. Res.*, 2017, **56**, 6945-6951.
10. L. Shi, C. Pang, S. Chen, M. Wang, K. Wang, Z. Tan, P. Gao, J. Ren, Y. Huang, H. Peng and Z. Liu, *Nano Lett.*, 2017, **17**, 3681-3687.
11. Y. Guo, G. Zhao, N. Wu, Y. Zhang, M. Xiang, B. Wang, H. Liu and H. Wu, *ACS Appl. Mater. Interfaces*, 2016, **8**, 34185-34193.
12. S. Balendhran, S. Walia, H. Nili, J. Z. Ou, S. Zhuiykov, R. B. Kaner, S. Sriram, M. Bhaskaran and K. Kalantar-zadeh, *Adv. Funct. Mater.*, 2013, **23**, 3952-3970.
13. M. Ghidui, J. Halim, S. Kota, D. Bish, Y. Gogotsi, M. W. Barsoum, *Chem. Mater.*, 2016, **28**, 3507-3514.
14. H. Zhang, *ACS Nano*, 2015, **9**, 9451-9469.
15. X. Zhou, Q. Zhang, L. Gan, H. Li, J. Xiong and T. Zhai, *Adv. Sci.*, 2016, **3**, 1600177.
16. F. F. Cui, C. Wang, X. B. Li, G. Wang, K. Q. Liu, Z. Yang, Q. L. Feng, X. Liang, Z. Y. Zhang, S. Z. Liu, Z. B. Lei, Z. H. Liu, H. Xu and J. Zhang, *Adv. Mater.*, 2016, **28**, 5019-5024.
17. Z. Y. Dai, X. X. Zang, J. Yang, C. C. Sun, W. L. Si, W. Huang and X. C. Dong, *ACS Appl. Mater. Interfaces*, 2015, **7**, 25396-25401.
18. W. Fu, F. H. Du, J. Su, X. H. Li, X. Wei, T. N. Ye, K. X. Wang and J. S. Chen, *Sci. Rep.*, 2014, **4**, 4673.
19. T. Fujita, Y. Ito, Y. W. Tan, H. Yamaguchi, D. Hojo, A. Hirata, D. Voiry, M. Chhowalla and M. W. Chen, *Nanoscale*, 2014, **6**, 12458-12462.
20. V. Eswaraiah, Q. Zeng, Y. Long and Z. Liu, *Small*, 2016, **12**, 3480-3502.
21. L. Song, Z. Liu, A. L. M. Reddy, N. T. Narayanan, J. Taha-Tijerina, J. Peng, G. H. Gao, J. Lou, R. Vajtai and P. M. Ajayan, *Adv. Mater.*, 2012, **24**, 4878-4895.
22. L. Ci, L. Song, C. H. Jin, D. Jariwala, D. X. Wu, Y. J. Li, A. Srivastava, Z. F. Wang, K. Storr, L. Balicas, F. Liu and P. M. Ajayan, *Nat. Mater.*, 2010, **9**, 430-435.
23. C. L. Tan, P. Yu, Y. L. Hu, J. Z. Chen, Y. Huang, Y. Q. Cai, Z. M. Luo, B. Li, Q. P. Lu, L. H. Wang, Z. Liu and H. Zhang, *J. Am. Chem. Soc.*, 2015, **137**, 10430-10436.
24. J. Liu, H. Wang, C. Fang, L. Fu and X. Qian, *Nano Lett.*, 2017, **17**, 467-475.
25. S. D. Lei, A. Sobhani, F. F. Wen, A. George, Q. Z. Wang, Y. H. Huang, P. Dong, B. Li, S. Najmaei, J. Bellah, G. Gupta, A. D. Mohite, L. H. Ge, J. Lou, N. J. Halas, R. Vajtai and P. Ajayan, *Adv. Mater.*, 2014, **26**, 7666-7672.
26. M.-W. Lin, H. L. Zhuang, J. Yan, T. Z. Ward, A. A. Puretzy, C. M. Rouleau, Z. Gai, L. Liang, V. Meunier, B. G. Sumpter, P. Ganesh, P. R. C. Kent, D. B. Geohegan, D. G. Mandrus and K. Xiao, *J. Mater. Chem. C*, 2016, **4**, 315-322.
27. P. A. Hu, Z. Z. Wen, L. F. Wang, P. H. Tan and K. Xiao, *ACS Nano*, 2012, **6**, 5988-5994.
28. S. D. Lei, L. H. Ge, S. Najmaei, A. George, R. Koppera, J. Lou, M. Chhowalla, H. Yamaguchi, G. Gupta, R. Vajtai, A. D. Mohite and P. M. Ajayan, *ACS Nano*, 2014, **8**, 1263-1272.
29. P. G. Yan, H. Chen, J. D. Yin, Z. H. Xu, J. R. Li, Z. K. Jiang, W. F. Zhang, J. Z. Wang, I. L. Li, Z. P. Sun and S. C. Ruan, *Nanoscale*, 2017, **9**, 1871-1877.
30. X. Zhou, N. Zhou, C. Li, H. Y. Song, Q. Zhang, X. Z. Hu, L. Gan, H. Q. Li, J. T. Lu, J. Luo, J. Xiong and T. Y. Zhai, *2D Mater.*, 2017, **4**, 025048.
31. O. Lopez-Sanchez, D. Lembke, M. Kayci, A. Radenovic and A. Kis, *Nat. Nanotechnol.*, 2013, **8**, 497-501.
32. R. B. Jacobs-Gedrim, M. Shanmugam, N. Jain, C. A. Durcan, M. T. Murphy, T. M. Murray, R. J. Matyi, R. L. Moore and B. Yu, *ACS Nano*, 2014, **8**, 514-521.
33. S. R. Tamalampudi, Y. Y. Lu, U. R. Kumar, R. Sankar, C. D. Liao, B. K. Moorthy, C. H. Cheng, F. C. Chou and Y. T. Chen, *Nano Lett.*, 2014, **14**, 2800-2806.
34. T. Maeda, W. Y. Gong and T. Wada, *Jpn. J. Appl. Phys.*, 2016, **55**, 04ES15.
35. B. Siberchicot, S. Jobic, V. Carreaux, P. Gressier and G. Ouvrard, *J. Phys. Chem.*, 1996, **100**, 5863-5867.
36. L. Britnell, R. M. Ribeiro, A. Eckmann, R. Jalil, B. D. Belle, A. Mishchenko, Y. J. Kim, R. V. Gorbachev, T. Georgiou, S. V. Morozov, A. N. Grigorenko, A. K. Geim, C. Casiraghi, A. H. Castro Neto and K. S. Novoselov, *Science*, 2013, **340**, 1311-1314.
37. B. L. Chittari, Y. Park, D. Lee, M. Han, A. H. MacDonald, E. Hwang and J. Jung, *Phys. Rev. B*, 2016, **94**, 184428.
38. A. H. Castro Neto, *Phys. Rev. Lett.*, 2001, **86**, 4382-4385.
39. D. Costanzo, S. Jo, H. Berger and A. F. Morpurgo, *Nat. Nanotechnol.*, 2016, **11**, 339-344.
40. R. F. Frindt, *Phys. Rev. Lett.*, 1972, **28**, 299-301.
41. Y. Ma, Y. Dai, M. Guo, C. Niu, Y. Zhu and B. Huang, *ACS Nano*, 2012, **6**, 1695-1701.
42. S. Lebègue, T. Björkman, M. Klintonberg, R. M. Nieminen and O. Eriksson, *Phys. Rev. X*, 2013, **3**, 031002.
43. J. Liu, S. Y. Park, K. F. Garrity and D. Vanderbilt, *Phys. Rev. Lett.*, 2016, **117**, 257201.
44. M. Zybert, M. Marchewka, E. M. Sheregii, D. G. Rickel, J. B. Betts, F. F. Balakirev, M. Gordon, A. V. Stier, C. H. Mielke, P. Pfeffer and W. Zawadzki, *Phys. Rev. B*, 2017, **95**, 115432.
45. H. L. Zhuang, Y. Xie, P. R. C. Kent and P. Ganesh, *Phys. Rev. B*, 2015, **92**, 035407.
46. Y. Fukuma, H. Asada, S. Senba and T. Koyanagi, *Appl. Phys. Lett.*, 2016, **108**, 222403.
47. Q. S. Zeng, H. Wang, W. Fu, Y. J. Gong, W. Zhou, P. M. Ajayan, J. Lou and Z. Liu, *Small*, 2015, **11**, 1868-1884.
48. T. A. Shifa, F. M. Wang, K. L. Liu, K. Xu, Z. X. Wang, X. Y. Zhan, C. Jiang and J. He, *Small*, 2016, **12**, 3802-3809.
49. Y. J. Gong, Z. Liu, A. R. Lupini, G. Shi, J. H. Lin, S. Najmaei, Z. Lin, A. L. Elias, A. Berkdemir, G. You, H.

- Terrones, M. Terrones, R. Vajtai, S. T. Pantelides, S. J. Pennycook, J. Lou, W. Zhou and P. M. Ajayan, *Nano Lett.*, 2014, **14**, 442-449.
50. J. F. Shen, J. Ji, P. Dong, R. Baines, Z. Q. Zhang, P. M. Ajayan and M. X. Ye, *J. Mater. Chem. A*, 2016, **4**, 8844-8850.
51. W. T. Zhang, X. D. Li, T. T. Jiang, J. L. Q. Song, Y. Lin, L. X. Zhu and X. L. Xu, *Nanoscale*, 2015, **7**, 13554-13560.
52. S. J. Zheng, L. F. Sun, T. T. Yin, A. M. Dubrovkin, F. C. Liu, Z. Liu, Z. X. Shen and H. J. Fan, *Appl. Phys. Lett.*, 2015, **106**.
53. S. D. Karande, N. Kaushik, D. S. Narang, D. Late and S. Lodha, *Appl. Phys. Lett.*, 2016, **109**, 142101.
54. B. Konkena, J. Masa, W. Xia, M. Muhler and W. Schuhmann, *Nano Energy*, 2016, **29**, 46-53.
55. M. Moustafa, A. Paulheim, M. Mohamed, C. Janowitz and R. Manzke, *Appl. Surf. Sci.*, 2016, **366**, 397-403.
56. A. K. Dasadia, B. B. Nariya and A. R. Jani, *J. Cryst. Growth*, 2015, **426**, 265-269.
57. A. Lapinska, A. Taube, M. Wasik, G. Z. Zukowska, A. Duzynska, J. Judek and M. Zdrojek, *J. Raman Spectrosc.*, 2017, **48**, 479-484.
58. P. Yu, J. H. Lin, L. F. Sun, Q. L. Le, X. C. Yu, G. H. Gao, C. H. Hsu, D. Wu, T. R. Chang, Q. S. Zeng, F. C. Liu, Q. J. Wang, H. T. Jeng, H. Lin, A. Trampert, Z. X. Shen, K. Suenaga and Z. Liu, *Adv. Mater.*, 2017, **29**, 1603991.
59. K. Z. Du, X. Z. Wang, Y. Liu, P. Hu, M. I. B. Utama, C. K. Gan, Q. H. Xiong and C. Kloc, *ACS Nano*, 2016, **10**, 1738-1743.
60. A. Villanueva, M. C. Morales-Varela and E. Ruiz-Hitzky, *Eur. J. Inorg. Chem.*, 2004, **2004**, 949-952.
61. J. D. Yao, Z. Q. Zheng and G. W. Yang, *ACS Appl. Mater. Interfaces*, 2016, **8**, 12915-12924.
62. V. Kiran, D. Mukherjee, R. N. Jenjeti and S. Sampath, *Nanoscale*, 2014, **6**, 12856-12863.
63. J. F. Shen, P. Dong, R. Baines, X. W. Xu, Z. Q. Zhang, P. M. Ajayan and M. X. Ye, *Chem. Commun.*, 2016, **52**, 9251-9254.
64. J. U. Lee, S. Lee, J. H. Ryoo, S. Kang, T. Y. Kim, P. Kim, C. H. Park, J. G. Park and H. Cheong, *Nano Lett.*, 2016, **16**, 7433-7438.
65. X. Wang, K. Du, Y. Y. F. Liu, P. Hu, J. Zhang, Q. Zhang, M. H. S. Owen, X. Lu, C. K. Gan and P. Sengupta, *2D Mater.*, 2016, **3**, 031009.
66. W. Toyoshima, T. Masubuchi, T. Watanabe, K. Takase, K. Matsubayashi, Y. Uwatoko and Y. Takano, *J. Phys.: Conf. Ser.*, 2009, **150**, 042215.
67. C. C. Mayorga-Martinez, Z. Sofer, D. Sedmidubsky, S. Huber, A. Y. S. Eng and M. Pumera, *ACS Appl. Mater. Interfaces*, 2017, **9**, 12563-12573.
68. N. Ismail, A. A. El-Meligi, Y. M. Temerk and M. Madian, *Int. J. Hydrogen Energy*, 2010, **35**, 7827-7834.
69. N. Ismail, Y. M. Temerk, A. A. El-Meligi, M. A. Badr and M. Madian, *J. Solid State Chem.*, 2010, **183**, 984-987.
70. D. Mukherjee, P. M. Austeria and S. Sampath, *ACS Energy Lett.*, 2016, **1**, 367-372.
71. Y. Gogotsi, *Nat. Mater.*, 2015, **14**, 1079-1080.
72. M. Naguib, M. Kurtoglu, V. Presser, J. Lu, J. J. Niu, M. Heon, L. Hultman, Y. Gogotsi and M. W. Barsoum, *Adv. Mater.*, 2011, **23**, 4248-4253.
73. O. Mashtalir, M. R. Lukatskaya, M. Q. Zhao, M. W. Barsoum and Y. Gogotsi, *Adv. Mater.*, 2015, **27**, 3501-3506.
74. R. Zeng, S. Q. Wang, G. D. Du, J. L. Wang, J. C. Debnath, P. Shamba, Z. Y. Fang and S. X. Dou, *J. Appl. Phys.*, 2012, **111**.
75. H. Falius, *Z. anorg. allg. Chem.*, 1968, **356**, 189-194.
76. O. Mashtalir, M. Naguib, B. Dyatkin, Y. Gogotsi and M. W. Barsoum, *Mater. Chem. Phys.*, 2013, **139**, 147-152.
77. M. Naguib, V. N. Mochalin, M. W. Barsoum and Y. Gogotsi, *Adv. Mater.*, 2014, **26**, 992-1005.
78. B. Anasori, M. R. Lukatskaya and Y. Gogotsi, *Nat. Rev. Mater.*, 2017, **2**, 16098.
79. M. Naguib, O. Mashtalir, J. Carle, V. Presser, J. Lu, L. Hultman, Y. Gogotsi and M. W. Barsoum, *ACS Nano*, 2012, **6**, 1322-1331.
80. B. Chen, F. Chang, J. Yang, H. Tang and C. Li, *Cryst. Res. Technol.*, 2014, **49**, 813-819.
81. L. Liu, J. Park, D. A. Siegel, K. F. McCarty, K. W. Clark, W. Deng, L. Basile, J. C. Idrobo, A. P. Li and G. Gu, *Science*, 2014, **343**, 163-167.
82. F. K. Ma, M. X. Wang, Y. L. Shao, L. J. Wang, Y. Z. Wu, Z. P. Wang and X. P. Hao, *J. Mater. Chem. C*, 2017, **5**, 2559-2565.
83. M. Ghidui, M. R. Lukatskaya, M.-Q. Zhao, Y. Gogotsi and M. W. Barsoum, *Nature*, 2014, **516**, 78-81.
84. J. Halim, S. Kota, M. R. Lukatskaya, M. Naguib, M. Q. Zhao, E. J. Moon, J. Pitock, J. Nanda, S. J. May and Y. Gogotsi, *Adv. Funct. Mater.*, 2016, **26**, 3118.
85. Z. W. Seh, K. D. Fredrickson, B. Anasori, J. Kibsgaard, A. L. Strickler, M. R. Lukatskaya, Y. Gogotsi, T. F. Jaramillo and A. Vojvodic, *ACS Energy Lett.*, 2016, **1**, 589-594.
86. A. Lipatov, M. Alhabeab, M. R. Lukatskaya, A. Boson, Y. Gogotsi and A. Sinitskii, *Adv. Electron. Mater.*, 2016, **2**, 1600255.
87. O. Mashtalir, M. Naguib, V. N. Mochalin, Y. Dall'Agnese, M. Heon, M. W. Barsoum and Y. Gogotsi, *Nat. Commun.*, 2013, **4**, 1716.
88. M. Naguib, R. R. Unocic, B. L. Armstrong and J. Nanda, *Dalton Trans.*, 2015, **44**, 9353-9358.
89. Y. Gogotsi, *Nat Mater*, 2015, **14**, 1079-1080.
90. Y. Miyamoto, A. Rubio, M. L. Cohen and S. G. Louie, *Phys. Rev. B*, 1994, **50**, 4976.
91. A. Rubio, J. L. Corkill and M. L. Cohen, *Phys. Rev. B*, 1994, **49**, 5081.
92. Z. Liu, L. L. Ma, G. Shi, W. Zhou, Y. J. Gong, S. D. Lei, X. B. Yang, J. N. Zhang, J. J. Yu, K. P. Hackenberg, A. Babakhani, J. C. Idrobo, R. Vajtai, J. Lou and P. M. Ajayan, *Nat. Nanotechnol.*, 2013, **8**, 119-124.
93. J. T. Jin, F. P. Pan, L. H. Jiang, X. G. Fu, A. M. Liang, Z. Y. Wei, J. Y. Zhang and G. Q. Sun, *ACS Nano*, 2014, **8**, 3313-3321.

94. Y. J. Gong, G. Shi, Z. H. Zhang, W. Zhou, J. Jung, W. L. Gao, L. L. Ma, Y. Yang, S. B. Yang, G. You, R. Vajtai, Q. F. Xu, A. H. MacDonald, B. I. Yakobson, J. Lou, Z. Liu and P. M. Ajayan, *Nat. Commun.*, 2014, **5**, 3193.
95. S. Zhang, J. Wu, Q. Yang, R. Tu, C. B. Wang, Q. Shen and L. M. Zhang, *AIP Adv.*, 2015, **5**, 047125.
96. C. J. Huang, C. Chen, M. W. Zhang, L. H. Lin, X. X. Ye, S. Lin, M. Antonietti and X. C. Wang, *Nat. Commun.*, 2015, **6**, 7698.
97. S. F. Zeng, W. L. Feng, H. Luo, Y. Q. Tan, Y. Wang, H. B. Zhang, T. Zhang and S. M. Peng, *Chem. Phys. Lett.*, 2017, **674**, 164-167.
98. T. Zhang, S. Zeng and G. Wen, *Mater. Lett.*, 2014, **132**, 277-280.
99. L. Massimi, M. G. Betti, S. Caramazza, P. Postorino, C. Mariani, A. Latini and F. Leardini, *Nanotechnology*, 2016, **27**, 435601.
100. Z. Han, G. Li, J. Tian and M. Gu, *Mater. Lett.*, 2002, **57**, 899-903.
101. X. R. Deng, H. Kousaka, T. Tokoroyama and N. Umehara, *Surf. Coat. Technol.*, 2014, **259**, 2-6.
102. Y. Chen, J. Xi, D. O. Dumcenco, Z. Liu, K. Suenaga, D. Wang, Z. Shuai, Y.-S. Huang and L. Xie, *ACS Nano*, 2013, **7**, 4610-4616.
103. C. Tan, W. Zhao, A. Chaturvedi, Z. Fei, Z. Zeng, J. Chen, Y. Huang, P. Ercius, Z. Luo, X. Qi, B. Chen, Z. Lai, B. Li, X. Zhang, J. Yang, Y. Zong, C. Jin, H. Zheng, C. Kloc and H. Zhang, *Small*, 2016, **12**, 1866-1874.
104. T. Tavsanoğlu, M. Jeandin and O. Addemir, *Surf. Eng.*, 2016, **32**, 755-760.
105. S. Beniwal, J. Hooper, D. P. Miller, P. S. Costa, G. Chen, S. Y. Liu, P. A. Dowben, E. C. H. Sykes, E. Zurek and A. Enders, *ACS Nano*, 2017, **11**, 2486-2493.
106. J. Wu, H. Yuan, M. Meng, C. Chen, Y. Sun, Z. Chen, W. Dang, C. Tan, Y. Liu, J. Yin, Y. Zhou, S. Huang, H. Q. Xu, Y. Cui, H. Y. Hwang, Z. Liu, Y. Chen, B. Yan and H. Peng, *Nat. Nanotechnol.*, 2017, **12**, 530-534.
107. Y. Shi, H. Li and L.-J. Li, *Chem. Soc. Rev.*, 2015, **44**, 2744-2756.
108. Q. Gong, L. Cheng, C. Liu, M. Zhang, Q. Feng, H. Ye, M. Zeng, L. Xie, Z. Liu and Y. Li, *ACS Catal.*, 2015, **5**, 2213-2219.
109. F. Liu, S. Zheng, A. Chaturvedi, V. Zolyomi, J. Zhou, Q. Fu, C. Zhu, P. Yu, Q. Zeng, N. D. Drummond, H. J. Fan, C. Kloc, V. I. Fal'ko, X. He and Z. Liu, *Nanoscale*, 2016, **8**, 5826-5834.
110. J. Xi, T. Zhao, D. Wang and Z. Shuai, *J. Phys. Chem. Lett.*, 2014, **5**, 285-291.
111. H. Li, X. Duan, X. Wu, X. Zhuang, H. Zhou, Q. Zhang, X. Zhu, W. Hu, P. Ren, P. Guo, L. Ma, X. Fan, X. Wang, J. Xu, A. Pan and X. Duan, *J. Am. Chem. Soc.*, 2014, **136**, 3756-3759.
112. Q. Feng, Y. Zhu, J. Hong, M. Zhang, W. Duan, N. Mao, J. Wu, H. Xu, F. Dong, F. Lin, C. Jin, C. Wang, J. Zhang and L. Xie, *Adv. Mater.*, 2014, **26**, 2648-2653.
113. H. Weyl, *Z. Phys.*, 1929, **56**, 330-352.
114. L. Huang, T. M. McCormick, M. Ochi, Z. Zhao, M.-T. Suzuki, R. Arita, Y. Wu, D. Mou, H. Cao, J. Yan, N. Trivedi and A. Kaminski, *Nat Mater*, 2016, **15**, 1155-1160.
115. I. Belopolski, S. Y. Xu, Y. Ishida, X. C. Pan, P. Yu, D. S. Sanchez, H. Zheng, M. Neupane, N. Alidoust, G. Q. Chang, T. R. Chang, Y. Wu, G. Bian, S. M. Huang, C. C. Lee, D. X. Mou, L. N. Huang, Y. Song, B. G. Wang, G. H. Wang, Y. W. Yeh, N. Yao, J. E. Rault, P. Le Fevre, F. Bertran, H. T. Jeng, T. Kondo, A. Kaminski, H. Lin, Z. Liu, F. Q. Song, S. Shin and M. Z. Hasan, *Phys. Rev. B*, 2016, **94**, 085127.
116. A. A. Soluyanov, D. Gresch, Z. Wang, Q. Wu, M. Troyer, X. Dai and B. A. Bernevig, *Nature*, 2015, **527**, 495-498.
117. G. Autès, D. Gresch, M. Troyer, A. A. Soluyanov and O. V. Yazyev, *Phys. Rev. Lett.*, 2016, **117**, 066402.
118. K. Koepf, D. Kasinathan, D. V. Efremov, S. Khim, S. Borisenko, B. Buchner and J. van den Brink, *Phys. Rev. B*, 2016, **93**, 201101(R).
119. R. Brec, D. M. Schleich, G. Ouvrard, A. Louisy and J. Rouxel, *Inorg. Chem.*, 1979, **18**, 1814-1818.
120. V. Nicolosi, M. Chhowalla, M. G. Kanatzidis, M. S. Strano and J. N. Coleman, *Science*, 2013, **340**, 1226419.
121. R. Brec, *Solid State Ionics*, 1986, **22**, 3-30.
122. J. Liu, X.-B. Li, D. Wang, W.-M. Lau, P. Peng and L.-M. Liu, *J. Chem. Phys.*, 2014, **140**, 054707.
123. H. Xiang, B. Xu, Y. Xia, J. Yin and Z. Liu, *RSC Adv.*, 2016, **6**, 89901-89906.
124. C. Sourisseau, J. P. Forgerit and Y. Mathey, *J. Solid State Chem.*, 1983, **49**, 134-149.
125. M. Scagliotti, M. Jouanne, M. Balkanski, G. Ouvrard and G. Benedek, *Phys. Rev. B*, 1987, **35**, 7097-7104.
126. P. Jernberg, S. Bjarman and R. Wäppling, *J. Magn. Magn. Mater.*, 1984, **46**, 178-190.
127. M. Khazaei, A. Ranjbar, M. Arai, T. Sasaki and S. Yunoki, *J. Mater. Chem. C*, 2017, **5**, 2488-2503.
128. V. M. Hong Ng, H. Huang, K. Zhou, P. S. Lee, W. Que, J. Z. Xu and L. B. Kong, *J. Mater. Chem. A*, 2017, **5**, 3039-3068.
129. M. Naguib, J. Halim, J. Lu, K. M. Cook, L. Hultman, Y. Gogotsi and M. W. Barsoum, *J. Am. Chem. Soc.*, 2013, **135**, 15966-15969.
130. B. Anasori, Y. Xie, M. Beidaghi, J. Lu, B. C. Hosler, L. Hultman, P. R. C. Kent, Y. Gogotsi and M. W. Barsoum, *ACS Nano*, 2015, **9**, 9507-9516.
131. M. Khazaei, A. Ranjbar, M. Arai and S. Yunoki, *Phys. Rev. B*, 2016, **94**, 125152.
132. R. Meshkian, Q. Tao, M. Dahlqvist, J. Lu, L. Hultman and J. Rosen, *Acta Mater.*, 2017, **125**, 476-480.
133. O. Stephan, P. M. Ajayan, C. Colliex, P. Redlich, J. M. Lambert, P. Bernier and P. Lefin, *Science*, 1994, **266**, 1683-1685.
134. J. Wu, H. Yuan, M. Meng, C. Chen, Y. Sun, Z. Chen, W. Dang, C. Tan, Y. Liu and J. Yin, *Nat. Nanotechnol.*, 2017, **12**, 530.
135. C. Gong, L. Li, Z. L. Li, H. W. Ji, A. Stern, Y. Xia, T. Cao, W. Bao, C. Z. Wang, Y. A. Wang, Z. Q. Qiu, R. J. Cava, S. G. Louie, J. Xia and X. Zhang, *Nature*, 2017, **546**, 265-269.

136. H. Pan, *J. Mater. Chem. A*, 2015, **3**, 21486-21493.
137. Y. Y. Peng, B. Akuzum, N. Kurra, M. Q. Zhao, M. Alhabe, B. Anasori, E. C. Kumbur, H. N. Alshareef, M. D. Ger and Y. Gogotsi, *Energy Environ. Sci.*, 2016, **9**, 2847-2854.
138. Q. Fu, J. Wen, N. Zhang, L. Wu, M. Zhang, S. Lin, H. Gao and X. Zhang, *RSC Adv.*, 2017, **7**, 11998-12005.
139. O. Mashtalir, M. Naguib, V. N. Mochalin, Y. Dall'Agnese, M. Heon, M. W. Barsoum and Y. Gogotsi, *Nat. Commun.*, 2013, **4**, 1716.
140. C. Eames and M. S. Islam, *J. Am. Chem. Soc.*, 2014, **136**, 16270-16276.
141. P. Kumar, H. Abuhimd, W. Wahyudi, M. L. Li, J. Ming and L. J. Li, *ECS J. Solid State Sci. Technol.*, 2016, **5**, Q3021-Q3025.
142. J. Yang, M. Naguib, M. Ghidui, L. M. Pan, J. Gu, J. Nanda, J. Halim, Y. Gogotsi and M. W. Barsoum, *J. Am. Ceram. Soc.*, 2016, **99**, 660-666.
143. A. H. Thompson and M. S. Whittingham, *Mater. Res. Bull.*, 1977, **12**, 741-744.
144. Y. V. Kuz'minskii, B. M. Voronin, I. M. Petrushina, N. N. Redin and G. P. Prikhodko, *J. Power Sources*, 1995, **55**, 1-6.
145. X. Peng, L. Peng, C. Wu and Y. Xie, *Chem. Soc. Rev.*, 2014, **43**, 3303-3323.
146. N. Choudhary, C. Li, H.-S. Chung, J. Moore, J. Thomas and Y. Jung, *ACS Nano*, 2016, **10**, 10726-10735.
147. J. Zhou, J. Qin, L. Guo, N. Zhao, C. Shi, E.-z. Liu, F. He, L. Ma, J. Li and C. He, *J. Mater. Chem. A*, 2016, **4**, 17370-17380.
148. S. Zhang, Z. Huang, Z. Wen, L. Zhang, J. Jin, R. Shahbazian-Yassar and J. Yang, *Nano Lett.*, 2017, **17**, 3518-3526.
149. P. C. K. Vesborg, B. Seger and I. Chorkendorff, *J. Phys. Chem. Lett.*, 2015, **6**, 951-957.
150. P. C. K. Vesborg and T. F. Jaramillo, *RSC Adv.*, 2012, **2**, 7933-7947.
151. K. C. Neyerlin, W. Gu, J. Jorne and H. A. Gasteiger, *J. Electrochem. Soc.*, 2007, **154**, B631-B635.
152. M. Zeng and Y. Li, *J. Mater. Chem. A*, 2015, **3**, 14942-14962.
153. H. Wang, R. Peng, Z. D. Hood, M. Naguib, S. P. Adhikari and Z. Wu, *ChemSusChem*, 2016, **9**, 1490-1497.
154. Z. Guo, J. Zhou, L. Zhu and Z. Sun, *J. Mater. Chem. A*, 2016, **4**, 11446-11452.
155. T. Y. Ma, J. L. Cao, M. Jaroniec and S. Z. Qiao, *Angew. Chem. Int. Ed.*, 2016, **55**, 1138-1142.
156. K. Xu, F. Wang, Z. Wang, X. Zhan, Q. Wang, Z. Cheng, M. Safdar and J. He, *ACS Nano*, 2014, **8**, 8468-8476.
157. K. Liu, F. Wang, K. Xu, T. A. Shifa, Z. Cheng, X. Zhan and J. He, *Nanoscale*, 2016, **8**, 4699-4704.
158. B. Hinnemann, P. G. Moses, J. Bonde, K. P. Jørgensen, J. H. Nielsen, S. Horch, I. Chorkendorff and J. K. Nørskov, *J. Am. Chem. Soc.*, 2005, **127**, 5308-5309.
159. T. F. Jaramillo, K. P. Jørgensen, J. Bonde, J. H. Nielsen, S. Horch and I. Chorkendorff, *Science*, 2007, **317**, 100-102.
160. J. Yang and H. S. Shin, *J. Mater. Chem. A*, 2014, **2**, 5979-5985.
161. D. Kong, J. J. Cha, H. Wang, H. R. Lee and Y. Cui, *Energy Environ. Sci.*, 2013, **6**, 3553-3558.
162. H. Tang, K. Dou, C.-C. Kaun, Q. Kuang and S. Yang, *J. Mater. Chem. A*, 2014, **2**, 360-364.
163. D. Voiry, H. Yamaguchi, J. Li, R. Silva, D. C. B. Alves, T. Fujita, M. Chen, T. Asefa, V. B. Shenoy, G. Eda and M. Chhowalla, *Nat Mater*, 2013, **12**, 850-855.
164. J. Lin, Z. Peng, G. Wang, D. Zakhidov, E. Larios, M. J. Yacaman and J. M. Tour, *Adv. Energy Mater.*, 2014, **4**, 1301875.
165. J. Xie, J. Zhang, S. Li, F. Grote, X. Zhang, H. Zhang, R. Wang, Y. Lei, B. Pan and Y. Xie, *J. Am. Chem. Soc.*, 2013, **135**, 17881-17888.